Thermally-activated hardening recovery in viscoplastic materials with kinematic hardening at high temperatures

Léo Thiercelin, Francis Praud, Fodil Meraghni *, Eric Fleury

Arts et Métiers Institute of Technology, CNRS, Université de Lorraine, LEM3-UMR 7239, F-57000, Metz, France

A B S T R A C T

In this work, a new constitutive model is proposed to describe the thermally-activated hardening recovery mechanism in metallic materials. This model takes up the concept of hardening recovery variable, which is extended to the case of kinematic hardening within a thermo-viscoplastic formulation including high temperature dependencies for both elastic and viscoplastic properties. The model is identified for AISI 316L austenitic stainless steel using experimental data from uni-axial tests conducted over a wide range of temperature (from room temperature to 1273 K) and at two different strain rates (2.5×10^{-4} and 2.5×10^{-3} s^{-1}). Validation is further achieved with rather good agreements by comparing the simulated responses with additional experimental data where the material is subjected to complex thermomechanical loading paths while other examples are presented to provide a better insight of the model and to illustrate its predictive capabilities.

1. Introduction

It is well-established that the properties of metals and alloys strongly depend on temperature. It is commonly established that the solicitations at high temperatures can have detrimental effects due to the reduction of strength properties, or the development of residual stresses, possibly resulting in material failure (Withers, 2007). However, in some other cases like in the annealing process or in hot metal forming, thermal exposure may be beneficial by helping the material to relax stresses (Totten et al., 2002; Angkurarach and Juijerm, 2020) and by promoting ductility (Humpreys et al., 2017). Whatever the purpose, to meet industrial challenges and needs, the thermomechanical behaviour of metallic materials must be well understood to accurately predict their response.

A wide variety of phenomenological and constitutive models have been developed over the past decades to address plastic and viscoplastic response of materials upon monotonic and cyclic loadings (Chaboche and Nouailhas, 1989; Lemaitre and Chaboche, 1990; Chaboche, 2008; Besson et al., 2010; Karvan and Varvani-Farahani, 2019b,a; Shekarian and Varvani-Farahani, 2019; Karvan and Varvani-Farahani, 2020). These models introduced different types of hardening, like isotropic, kinematic or combined with temperature-dependent parameters to capture the rate- and temperature-dependent non-linear behaviour of metallic materials.

The temperature dependence of the material parameters reflects microstructural changes and the activation of various physical phenomena taking place at the microscopic scale. Among them, the hardening recovery is a particular phenomenon that enables the material to partially or fully restore its initial properties upon thermal exposures, as the result of dislocations rearrangement and annihilation, grain recrystallization and their subsequent growth (Humphreys, 1997; Humpreys et al., 2017), as illustrated in Fig. 1.

Several phenomenological models have been proposed to integrate the annealing under temperature exposures. Commonly used models consider the existence of an activation temperature from which the hardening recovery is complete or initiated. In this case, the hardening variables are artificially reset to zero (Muránsky et al., 2012a,b; Deng et al., 2017). In other models, two annealing stages are considered: a starting temperature for partial recovery and another one, beyond which the recovery is total and instantaneous. Despite predictive results (Hendili, 2016; Depradeux and Coquard, 2018), these approaches display a lack of physical consistency, since they only consider the recovery mechanism when a certain temperature is reached without accounting for the time of exposure.

Recrystallization models based on Johnson–Mehl–Avrami–Kolmogrov laws have also been developed (Avrami, 1939, 1940; Fanfoni and Tomellini, 1998). These models are often limited to simple heat treatments like isothermal conditions or anisothermal with constant heating rates, and are hence not applicable to practical real cases.

* Corresponding author.
E-mail address: fodil.meraghni@ensam.eu (F. Meraghni).

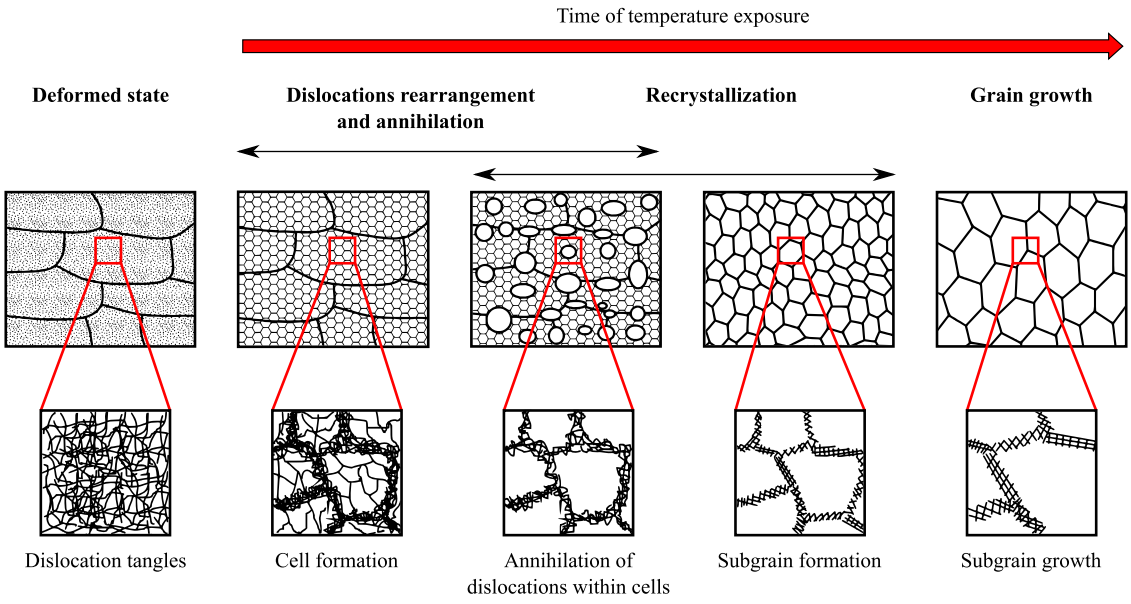

Fig. 1. Representation of the microstructural mechanisms behind the thermally-activated hardening recovery phenomenon. Namely: dislocations rearrangement and annihilation, grain recrystallization and their subsequent growth.
Source: Figure adapated from Humpreys et al. (2017).

Nevertheless, Suo et al. (2020) have recently proposed a time- and temperature- dependent corrective factor directly derived from the Avrami's equation to correct the kinematic hardening variable of their model.

One can also mention the dislocation-based models that represent the competition between annihilation and creation of dislocations under the combined effects of stress and temperature (Mecking and Kocks, 1981; Estrin and Mecking, 1984; Kocks and Mecking, 2003; Blaizot et al., 2016; Lin et al., 2018; Yuan et al., 2019; Voyiadjis and Abed, 2005; Voyiadjis et al., 2019). Since these models involve dislocation physics, they rather well describe the recovery mechanism. However, the identification of those models remains quite cumbersome and requires non-conventional experimental techniques to quantify the dislocation density and to follow their kinetics during the tests, *e.g.*, Transmission Electron Microscopy. Moreover, the hardening recovery is not only related to the annihilation of dislocations, particularly in metals with low stacking fault energy, such as austenitic stainless steel, since the recrystallization and the dislocations annihilation seem to occur simultaneously (Humpreys et al., 2017).

In an alternative approach, some of the authors of this paper has previously introduced the concept of hardening recovery variable within a classical elastoplastic formulation with isotropic hardening (Mouelle et al., 2020). The main idea behind this concept is to consider an internal state variable, referred to as the recovery variable, that gradually counteracts the effect of the hardening through a temperature-dependent evolution law. Although this model was able to capture some interesting tendencies, some features are still clearly missing to properly reproduce the material responses at high temperatures (Mouelle, 2020). This was mainly caused by the fact that, the hardening recovery was only formulated in the case of isotropic hardening without any other time- or temperature-dependencies with regards to the elasto-plastic properties. Indeed, isotropic hardening is not always appropriate to well describe the material behaviour upon alternate tension–compression. Such loading conditions are common in metal-forming applications like in multi-pass welding. Moreover, accounting for time- and temperature-dependencies appears to be necessary to well describe the material behaviour at moderate and high temperatures, even when the hardening recovery is not yet active.

Therefore, to address these issues, a new constitutive model is proposed in this work. The latter takes up the concept of the hardening recovery variable, but extends it to the case of kinematic hardening. The model is formulated considering an elasto-viscoplastic formulation since it is well established that metallic materials exhibit viscous effects at high temperatures. Furthermore, temperature dependencies are set in the elastic and viscoplastic properties to account for the prevailing thermal influences on the material response. The model is then identified for AISI 316L austenitic stainless steel using experimental data from Depradeux (2004) and Hendili (2016), who conducted uni-axial tension tests over a wide range of temperature (from room temperature to 1273 K) and at two different strain rates (2.5×10^{-4} and 2.5×10^{-3} s^{-1}). Validation is further achieved with rather good agreements by comparing the simulated responses with additional experimental data (Depradeux, 2004) where the material is subjected to complex thermomechanical loading paths including tension-relaxation and fully constrained dilatation tests. Other examples are presented to provide a better insight of the model, as well as to illustrate the kinetic of the hardening recovery in relation with the temperature and the time of exposure.

In this work, the following notation is adopted: bold and blackboard symbols denote second and fourth order tensors, respectively, whereas other symbols are scalar quantities. The product operators : and $\otimes$ depict the twice contracted and the dyadic products, respectively, such as:

$$[\boldsymbol{A} : \boldsymbol{B}] = A_{ij}B_{ij}, \qquad [\mathbb{A} : \boldsymbol{B}]_{ij} = A_{ijkl}B_{kl}, \qquad [\boldsymbol{A} \otimes \boldsymbol{B}]_{ijkl} = A_{ij}B_{kl}.$$

Moreover, all the second order tensors are symmetric ($A_{ij} = A_{ji}$) and all the fourth order tensors have at least the minor symmetries ($A_{ijkl} = A_{jikl} = A_{ijlk}$). Consequently, they can be respectively reduced to 6×1 and 6×6 matrices according to the Voigt notation. $\boldsymbol{I}$ and $\mathbb{I}$ stand for the second and fourth order identity tensors, respectively. The positive part of a scalar quantity a is denoted by $\langle a \rangle_+$, such that $\langle a \rangle_+ = a$ if $a \geq 0$ or $\langle a \rangle_+ = 0$ if $a < 0$. The operators $\mathrm{hyd}(\boldsymbol{\sigma})$ and $\mathbf{Dev}(\boldsymbol{\sigma})$ designate the hydrostatic pressure and the deviatoric part of a stress tensor $\boldsymbol{\sigma}$, respectively:

$$\mathrm{hyd}(\boldsymbol{\sigma}) = \frac{1}{3}\mathrm{tr}(\boldsymbol{\sigma}), \qquad \mathbf{Dev}(\boldsymbol{\sigma}) = \boldsymbol{\sigma} - \mathrm{hyd}(\boldsymbol{\sigma})\boldsymbol{I},$$

while $\mathrm{eq}(\boldsymbol{\sigma})$ is the equivalent von Mises stress:

$$\mathrm{eq}(\boldsymbol{\sigma}) = \sqrt{\frac{3}{2}\mathbf{Dev}(\boldsymbol{\sigma}) : \mathbf{Dev}(\boldsymbol{\sigma})}.$$

2. Constitutive equations and thermodynamic framework

2.1. State laws

The proposed constitutive equations are based on a viscoplastic model with kinematic hardening (Lemaitre and Chaboche, 1990). Accordingly, the energetic state of the material is described by the following form of the Helmholtz free energy potential:

$$\rho\psi(\boldsymbol{\varepsilon}, T, \boldsymbol{\varepsilon}_p, \boldsymbol{\xi}_p, \boldsymbol{\xi}_r) = \frac{1}{2}\Big(\boldsymbol{\varepsilon} - \boldsymbol{\varepsilon}_p - \boldsymbol{\varepsilon}_{th}(T)\Big) : \mathbb{C}(T) : \Big(\boldsymbol{\varepsilon} - \boldsymbol{\varepsilon}_p - \boldsymbol{\varepsilon}_{th}(T)\Big) + \frac{c(T)}{2}(\boldsymbol{\xi}_p - \boldsymbol{\xi}_r) : (\boldsymbol{\xi}_p - \boldsymbol{\xi}_r) + \rho\psi_{th}(T), \tag{1}$$

which involves the total strain $\boldsymbol{\varepsilon}$ and the absolute temperature T as observable state variables. Furthermore, the Helmholtz free energy also depends on a set of internal state variables, among which are the plastic strain $\boldsymbol{\varepsilon}_p$, the back strain $\boldsymbol{\xi}_p$ and the back strain recovery variable $\boldsymbol{\xi}_r$, simply referred to as recovery variable.

In (1), ρ denotes the mass density considered as constant under the small strains assumption. $\mathbb{C}(T)$ is a temperature-dependent fourth order material stiffness tensor defined as:

$$\mathbb{C}(T) = g_e(T)\ \mathbb{C}_0, \tag{2}$$

where $\mathbb{C}_0$ is the stiffness tensor at the reference temperature T_0, classically defined for bulk isotropic materials by E_0 and ν_0, the Young modulus and the Poisson ratio, respectively. Note that, in this work, the reference temperature is the room temperature such that $T_0 = 293$ K. As written in (2), the elastic stiffness at a given temperature is connected to the one at the reference temperature through a shift function $g_e(T)$ that will be defined later in Section 3. This function is equal to 1 at the reference temperature and tends to 0 for high temperatures. Similarly to the elastic stiffness, $c(T)$ is a temperature-dependent hardening parameter defined as:

$$c(T) = g_p(T)\ c_0, \tag{3}$$

where c_0 is the hardening parameter given at the reference temperature, while $g_p(T)$ is another temperature-dependent shift function associated with plasticity. Like $g_e(T)$, $g_p(T)$ is equal to 1 at the reference temperature whereas it tends to 0 for high temperatures. Its expression will also be defined later in Section 3. $\boldsymbol{\varepsilon}_{th}(T)$ stands for the thermal strain, usually expressed for an isotropic material as:

$$\boldsymbol{\varepsilon}_{th}(T) = \alpha \boldsymbol{I}(T - T_0), \tag{4}$$

where α denotes the coefficient of thermal expansion. The last term of (1), namely: $\psi_{th}(T)$, represents the calorific energy, which depends on the temperature. Its expression is given by:

$$\psi_{th}(T) = c_p\left[(T - T_0) - T\ln\left(\frac{T}{T_0}\right)\right] - s_0 T + e_0, \tag{5}$$

where s_0 and e_0 are the entropy and the internal energy at the reference temperature T_0, whereas c_p denotes the specific heat capacity at constant pressure.

By following the standard thermodynamic derivation, it yields for the stress:

$$\boldsymbol{\sigma} = \rho\frac{\partial\psi}{\partial\boldsymbol{\varepsilon}} = \mathbb{C}(T) : \big(\boldsymbol{\varepsilon} - \boldsymbol{\varepsilon}_p - \boldsymbol{\varepsilon}_{th}(T)\big), \qquad -\boldsymbol{\sigma} = \rho\frac{\partial\psi}{\partial\boldsymbol{\varepsilon}_p}, \tag{6}$$

and for the back stress:

$$\boldsymbol{X} = \rho\frac{\partial\psi}{\partial\boldsymbol{\xi}_p} = c(T)(\boldsymbol{\xi}_p - \boldsymbol{\xi}_r), \qquad -\boldsymbol{X} = \rho\frac{\partial\psi}{\partial\boldsymbol{\xi}_r}. \tag{7}$$

Furthermore, the specific entropy per mass unit s is associated to the temperature such that:

$$s = -\frac{\partial\psi}{\partial T}. \tag{8}$$

The state and associated variables are summarized in Table 1.

Table 1
State and associated variables. The present formulation involves the total strain $\boldsymbol{\varepsilon}$ and the absolute temperature T as observable state variables, to which the stress $\boldsymbol{\sigma}$ and the specific entropy s, respectively, are associated. Furthermore, the plastic strain $\boldsymbol{\varepsilon}_p$, the back strain $\boldsymbol{\xi}_p$ and the recovery variable $\boldsymbol{\xi}_r$ are involved as internal state variables, to which $-\boldsymbol{\sigma}$, the back stress $\boldsymbol{X}$ and $-\boldsymbol{X}$, respectively, are associated.

State variables		Associated variables
Observable	Internal	–
$\boldsymbol{\varepsilon}$		$\boldsymbol{\sigma}$
T		s
	$\boldsymbol{\varepsilon}_p$	$-\boldsymbol{\sigma}$
	$\boldsymbol{\xi}_p$	$\boldsymbol{X}$
	$\boldsymbol{\xi}_r$	$-\boldsymbol{X}$

Note that, unlike classical kinematic hardening formulations, the back stress $\boldsymbol{X}$ does not only depend on $\boldsymbol{\xi}_p$, but rather on the difference between the $\boldsymbol{\xi}_p$ and $\boldsymbol{\xi}_r$, as given in Eq. (7). Thus, through its evolution, the recovery variable $\boldsymbol{\xi}_r$ will play an antagonistic role with regard to the back strain $\boldsymbol{\xi}_p$, by gradually cancelling the effect of the hardening when $\boldsymbol{\xi}_r$ gets close to $\boldsymbol{\xi}_p$. This process will be further detailed later in Section 2.2.2.

2.2. Evolution laws

To guaranty the thermodynamic admissibility, it is important that the evolution laws, expressing the kinetic of the internal state variables, are well in line with the Clausius–Duhem inequality, stating that the intrinsic dissipation must be positive or null. For the proposed formulation, this gives:

$$\begin{aligned}\dot{\Phi} &= \boldsymbol{\sigma} : \dot{\boldsymbol{\varepsilon}} - \rho(\dot{\psi} + s\dot{T}) \geq 0\\ &= \boldsymbol{\sigma} : \dot{\boldsymbol{\varepsilon}} - \rho\left(\frac{\partial\psi}{\partial\boldsymbol{\varepsilon}} : \dot{\boldsymbol{\varepsilon}} + \frac{\partial\psi}{\partial T}\dot{T} + \frac{\partial\psi}{\partial\boldsymbol{\varepsilon}_p} : \dot{\boldsymbol{\varepsilon}}_p + \frac{\partial\psi}{\partial\boldsymbol{\xi}_p} : \dot{\boldsymbol{\xi}}_p + \frac{\partial\psi}{\partial\boldsymbol{\xi}_r} : \dot{\boldsymbol{\xi}}_r + s\dot{T}\right) \geq 0\\ &= \boldsymbol{\sigma} : \dot{\boldsymbol{\varepsilon}}_p - \boldsymbol{X} : \dot{\boldsymbol{\xi}}_p + \boldsymbol{X} : \dot{\boldsymbol{\xi}}_r \geq 0.\end{aligned} \tag{9}$$

In the above equation, two contributions can be identified: the dissipation associated with viscoplasticity, *i.e.*, $\boldsymbol{\sigma} : \dot{\boldsymbol{\varepsilon}}_p - \boldsymbol{X} : \dot{\boldsymbol{\xi}}_p$, and the one associated with the hardening recovery, *i.e.*, $\boldsymbol{X} : \dot{\boldsymbol{\xi}}_r$. Since, the viscoplasticity and the hardening recovery mechanism may occur independently from one another, each of these two contributions must be positive or null. For these reasons, two potential functions will be used to derive the evolution laws, one for the viscoplasticity, and another for the hardening recovery.

2.2.1. Viscoplasticity with kinematic hardening

Non-linear kinematic hardening (Armstrong and Frederick, 1966) is commonly employed to represent the asymmetrical behaviour of metallic material, *i.e.*, the Bauschinger effect, upon alternate tension/compression loading stages. Such type of hardening necessitates to be formulated in the context of non-associative plasticity. Accordingly, the evolution laws derive from the normality rule of a convex indicative potential function defined as:

$$F(\boldsymbol{\sigma}, \boldsymbol{X}; T) = f(\boldsymbol{\sigma}, \boldsymbol{X}, T) + \frac{\gamma}{2\,c(T)}\boldsymbol{X} : \boldsymbol{X} \tag{10}$$

where γ is an additional hardening parameter, which is assumed to be temperature-independent, while $f(\boldsymbol{\sigma}, \boldsymbol{X}, T)$ represents the yield function given by:

$$f(\boldsymbol{\sigma}, \boldsymbol{X}, T) = \mathrm{eq}(\boldsymbol{\sigma} - \boldsymbol{X}) - \sigma_y(T). \tag{11}$$

One can notice that the yield function depends on the temperature through the yield threshold $\sigma_y(T)$, which is defined as:

$$\sigma_y(T) = g_p(T)\,\sigma_{y_0}. \tag{12}$$

Like the expression of the hardening parameter $c(T)$ in (3), the temperature dependency of $\sigma_y(T)$ is expressed by multiplying the yield threshold at the reference temperature σ_{y_0} by the same shift function $g_p(T)$.

Following the normality rule of $F(\boldsymbol{\sigma}, \boldsymbol{X}; T)$, it yields for the evolution laws:

$$\dot{\boldsymbol{\epsilon}}_p = \frac{\partial F}{\partial \boldsymbol{\sigma}} \dot{p} = \boldsymbol{\Lambda}(\boldsymbol{\sigma}, \boldsymbol{X})\, \dot{p}, \qquad \dot{\boldsymbol{\xi}}_p = -\frac{\partial F}{\partial \boldsymbol{X}} \dot{p} = \boldsymbol{\Omega}(\boldsymbol{\sigma}, \boldsymbol{X}, T)\, \dot{p}, \tag{13}$$

where p is a multiplier ($\dot{p} \geq 0$), whereas $\boldsymbol{\Lambda}(\boldsymbol{\sigma}, \boldsymbol{X})$ and $\boldsymbol{\Omega}(\boldsymbol{\sigma}, \boldsymbol{X}, T)$ respectively denote the plastic strain and back strain flows:

$$\boldsymbol{\Lambda}(\boldsymbol{\sigma}, \boldsymbol{X}) = \frac{3}{2} \frac{\mathbf{Dev}(\boldsymbol{\sigma} - \boldsymbol{X})}{\mathrm{eq}(\boldsymbol{\sigma} - \boldsymbol{X})}, \qquad \boldsymbol{\Omega}(\boldsymbol{\sigma}, \boldsymbol{X}, T) = \boldsymbol{\Lambda}(\boldsymbol{\sigma}, \boldsymbol{X}) - \frac{\gamma}{c(T)} \boldsymbol{X}. \tag{14}$$

Note that the convexity of the indicative function F with regard to the associated variables guarantees that the plasticity-related dissipation is always positive or null, *i.e.*, $\boldsymbol{\sigma} : \dot{\boldsymbol{\epsilon}}_p - \boldsymbol{X} : \dot{\boldsymbol{\xi}}_p \geq 0$.

To account for a viscoplastic behaviour, the evolution of the multiplier p is connected to the yield function $f(\boldsymbol{\sigma}, \boldsymbol{X}, T)$ through a Norton-like law (Norton, 1929):

$$\dot{p} = \frac{1}{\eta} \left[\frac{\langle f(\boldsymbol{\sigma}, \boldsymbol{X}, T) \rangle_+}{\sigma_y(T)} \right]^N \tag{15}$$

where η, N are viscosity parameters. It is worth noticing that in the above equation, the yield function is normalized by the yield threshold $\sigma_y(T)$, which itself depends on the temperature through the shift function $g_p(T)$, as defined in Eq. (12). In this manner, $g_p(T)$ acts as a unique temperature-dependent function for the whole viscoplasticity mechanism.

2.2.2. *Thermally-activated hardening recovery*

The recovery kinetic is mainly governed by the temperature T and the dislocation density (Petkovic et al., 1979; Farzadi, 2015; Mouelle et al., 2020). From a phenomenological standpoint, the hardening, through the back stress $\boldsymbol{X}$, can be considered as a representative quantity of the actual dislocation density. For these reasons, T and $\boldsymbol{X}$ are considered as driving forces of the hardening recovery process. To this end, the recovery kinetic is based on a dual dissipation potential defined as a convex function of the back stress and in which the temperature acts as parameter. This gives:

$$\varphi_r^*(\boldsymbol{X}; T) = g_r(T)\, \frac{A_X}{2} \boldsymbol{X} : \boldsymbol{X}, \tag{16}$$

where A_X is an amplitude parameter and $g_r(T)$ is an activation function of the recovery mechanism. The latter is formulated using a Johnson–Mehl–Avrami–Kolmogorov-like law (JMAK) (Avrami, 1939, 1940; Fanfoni and Tomellini, 1998):

$$g_r(T) = \exp\left(-\left(\frac{T_r}{T} \right)^{n_r} \right). \tag{17}$$

This form is motivated by the fact that the hardening covers not only the annihilation of dislocations but also the grain recrystallization whose effects are well predicted by the JMAK laws. Fig. 2 shows that, in $g_r(T)$, T_r represents a transition temperature from which the recovery process becomes predominant, whereas n_r is a sensitivity parameter regarding this transition.

The evolution law of the recovery variable is then achieved after derivation of this potential with respect to its associated variable, *i.e.*, $-\boldsymbol{X}$. accordingly, it yields:

$$\dot{\boldsymbol{\xi}}_r = \frac{\partial \varphi_r^*}{\partial \boldsymbol{X}} = g_r(T) A_X \boldsymbol{X}. \tag{18}$$

With this formalism, the hardening recovery variable rate is nearly null when the temperature is far below the transition temperature T_r, as $g_r(T \ll T_r) \to 0$, making the recovery mechanism quasi-inactive at low temperatures. However, the recovery mechanism starts becoming significantly active when the temperature approaches T_r and eventually becomes fully active, when the temperature is far beyond T_r, as $g_r(T \gg T_r) \to 1$. The hardening recovery variable rate is further amplified by the actual value of $\boldsymbol{X}$ through the parameter A_X.

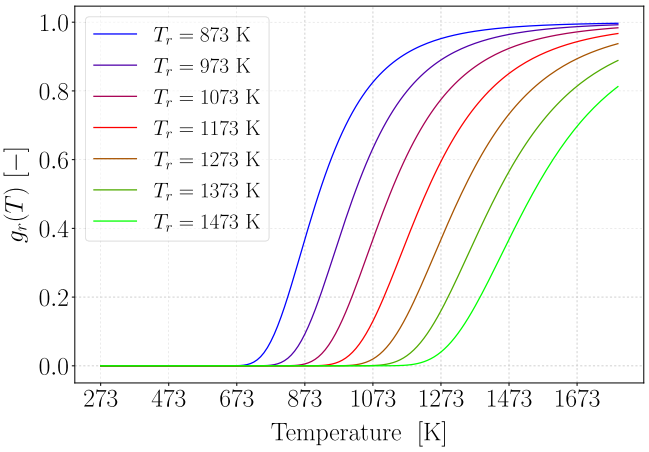

(a) Function $g_r(T)$ for various values of T_r at $n_r = 8$.

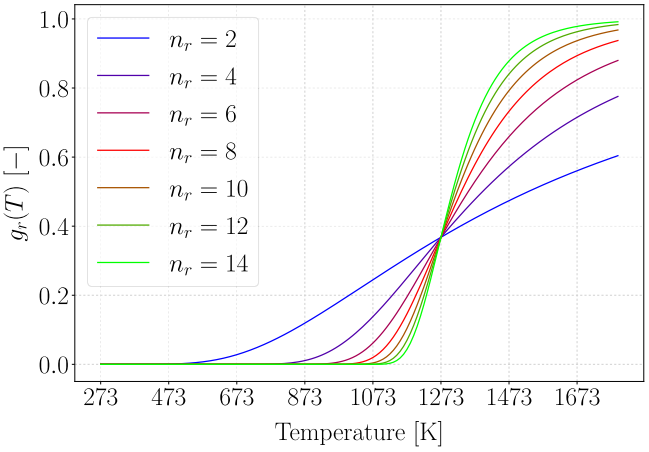

(b) Function $g_r(T)$ for various values of n_r at $T_r = 1273$ K.

Fig. 2. Activation function of the recovery mechanism $g_r(T)$. This function involves two parameters, namely: a transition temperature T_r and n_r, a sensitivity parameter regarding this transition.

Note that the convexity of $\varphi_r^*(\boldsymbol{X}; T)$ necessarily implies that the hardening recovery-related dissipation is positive or null, *i.e.*, $\boldsymbol{X} : \dot{\boldsymbol{\xi}}_r \geq 0$, making the proposed constitutive relation well thermodynamically admissible.

2.3. *Description of the hardening recovery mechanism*

During the hardening recovery, $\boldsymbol{\xi}_r$ runs towards $\boldsymbol{\xi}_p$ as a result of a temperature exposure. This process can be emphasized by combining Eqs. (7) and (18) together such that:

$$\boldsymbol{\xi}_r + \tau_r(T)\, \dot{\boldsymbol{\xi}}_r = \boldsymbol{\xi}_p. \tag{19}$$

This equation appears to be a first order differential equation highlighting a temperature-dependent characteristic time $\tau_r(T)$ that can be identified as:

$$\tau_r(T) = \frac{1}{c(T) g_r(T) A_X}, \tag{20}$$

where $c(T)$ and $g_r(T)$ are given in Eqs. (3) and (17), respectively. $\tau_r(T)$ provides a useful information about which range of time the hardening recovery is expected to occur, for a given temperature. One can notice that when the recovery mechanism is quasi-inactive at low temperatures, τ_r tends to very long times whereas it becomes

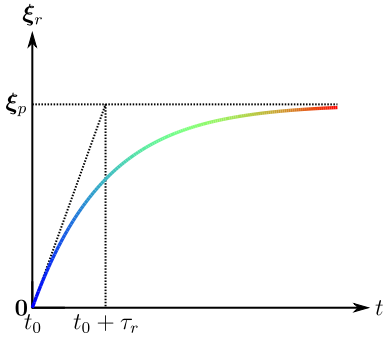

(a) The hardening recovery variable $\boldsymbol{\xi}_r$ asymptotically tends to $\boldsymbol{\xi}_p$.

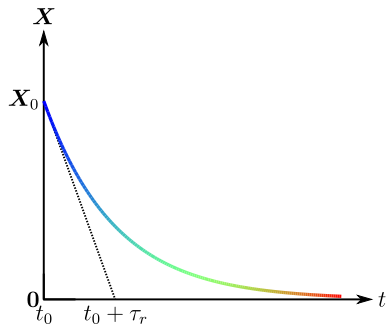

(b) The back stress $\boldsymbol{X}$ relaxes to zero, since $\boldsymbol{X}$ is proportional to the difference between $\boldsymbol{\xi}_p$ and $\boldsymbol{\xi}_r$.

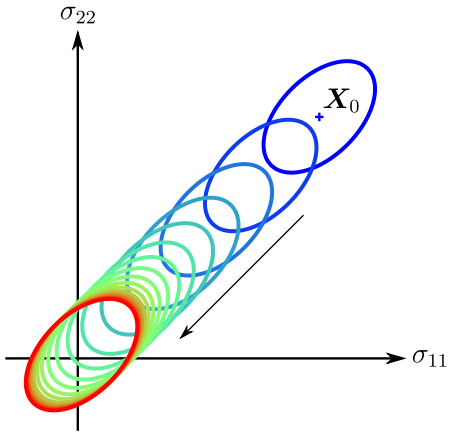

(c) The yield function is gradually shifted back to the stress space centre as the back stress relaxes to zero.

Fig. 3. Illustrative case of an already yielded material, undergoing hardening recovery without any active yielding, *i.e.*, $\boldsymbol{\xi}_p \neq \mathbf{0}$ and $\dot{\boldsymbol{\xi}}_p = \mathbf{0}$, as a result of a sudden temperature exposure held constant, *i.e.*, $\dot{T} = 0$, from an instant t_0.

much shorter when the hardening recovery becomes active at higher temperatures.

Let us consider the case of an already yielded material, undergoing hardening recovery without any active yielding, *i.e.*, $\boldsymbol{\xi}_p \neq \mathbf{0}$ and $\dot{\boldsymbol{\xi}}_p = \mathbf{0}$, as a result of a sudden temperature exposure held constant, *i.e.*, $\dot{T} = 0$, from an instant t_0. Under these conditions, Fig. 3(a) then shows that $\boldsymbol{\xi}_r$ asymptotically tends to $\boldsymbol{\xi}_p$ through an exponential growth:

$$\boldsymbol{\xi}_r(t;T) = \boldsymbol{\xi}_p\left(1 - \exp\left(-\frac{t-t_0}{\tau_r(T)}\right)\right). \tag{21}$$

According to Eq. (7), since the back stress $\boldsymbol{X}$, for a given temperature, is proportional to the difference between $\boldsymbol{\xi}_p$ and $\boldsymbol{\xi}_r$, Fig. 3(b) shows that $\boldsymbol{X}$ relaxes to zero by following an exponential decay:

$$\boldsymbol{X}(t;T) = \boldsymbol{X}_0(T) \times \exp\left(-\frac{t-t_0}{\tau_r(T)}\right), \qquad \text{with} \qquad \boldsymbol{X}_0(T) = c(T)\boldsymbol{\xi}_p, \tag{22}$$

gradually shifting the yield function, in Eq. (11), back to the stress space centre, as illustrated in Fig. 3(c). Note that according to Eqs. (21) or (22), $3 \times \tau_r$ represents to time needed to recover 95 % of the hardening. It is worth noticing that a similar trend is obtained with the Zener–Wert–Avrami equation that is commonly utilized to predict the thermal relaxation of residual stresses (Totten et al., 2002; Angkurarach and Juijerm, 2020).

2.4. Assumption regarding the temperature field equation

The energy balance equation governs the temperature field within the material domain. By combining together the first law of thermodynamics in its local form with the Fourier law, one obtains for an isotropic medium:

$$r + \omega + k\boldsymbol{\nabla}_{\boldsymbol{x}}^2 T = 0, \tag{23}$$

where ω stands for an eventual applied heat source, k is the material conductivity and $\boldsymbol{\nabla}_{\boldsymbol{x}}^2$ the Laplace operator. Furthermore, r represents the differential energy density rate between the mechanical power and the rate of internal energy. Knowing that the latter is connected to the Helmholtz free energy by $e = \psi + Ts$, it yields for r:

$$\begin{aligned} r &= \boldsymbol{\sigma} : \dot{\boldsymbol{\varepsilon}} - \rho\dot{e} \qquad \text{with} \qquad \dot{e} = \dot{\psi} + s\dot{T} + T\dot{s} \\ &= \boldsymbol{\sigma} : \dot{\boldsymbol{\varepsilon}} - \rho(\dot{\psi} + s\dot{T}) - \rho T\dot{s}, \\ &= \dot{\boldsymbol{\Phi}} - \rho T\dot{s} \end{aligned} \tag{24}$$

where the intrinsic dissipation $\dot{\boldsymbol{\Phi}}$ is given in (9) for the proposed model formulation.

According to (23) and (24), It is clear that the deformation as well as the hardening recovery processes obviously play a role in the energy balance through the energy dissipated by the material and the variation of entropy, resulting in temperature changes within the material. This makes the mechanical and thermal problems interdependent such that

they should be solved through a fully-coupled thermomechanical analysis, where the equilibrium equations (mechanical problem) and the energy balance equation (thermal problem) are simultaneously solved, while integrating all the coupling terms as detailed in Chatzigeorgiou et al. (2016, 2018). However, since the temperature sensitivity of metallic materials is usually quite low compared to the temperature elevations that can be caused by the intrinsic dissipation, its effect can be neglected in the expression of r, *i.e.*, $\dot{\Phi} \approx 0$. Moreover, it can also be assumed that most of the entropy results from the differentiation of the caloric energy ψ_{th}, given in (5), with respect to the temperature. Therefore, since ψ_{th} only depends on the temperature, it yields:

$$s = -\frac{\partial \psi}{\partial T} \approx -\frac{\partial \psi_{th}}{\partial T} \qquad \Rightarrow \qquad \dot{s} \approx -\frac{\partial^2 \psi_{th}}{\partial T^2}\dot{T} = c_p \frac{\dot{T}}{T}. \tag{25}$$

With these two assumptions in mind, the differential energy density rate reduces to:

$$r \approx -\rho c_p \dot{T}, \tag{26}$$

which renders the thermal problem independent from the mechanical one. In this context, the whole problem can be conveniently treated by means of an uncoupled thermomechanical analysis, where the thermal problem is first solved prior to the mechanical one. The temperature field computed from the thermal analysis is then utilized as input data for the subsequent mechanical analysis. In that sense, the temperature can be regarded as a controllable quantity, as considered in the remainder of this paper.

2.5. Numerical implementation

It is important to remind that a FE solver, like *ABAQUS/Standard*, employs a backward Euler (or time-implicit) integration scheme. Accordingly, a constitutive law is implemented through an integrator, *e.g.*, a UMAT (User MATerial subroutine) in *ABAQUS/Standard*, that computes:

(i) The stress as well as history-dependent quantities (internal state variables) over a time increment $[t^{(n)}; t^{(n+1)}]$ of length $\Delta t = t^{(n+1)} - t^{(n)}$, while all variables known at $t^{(n)}$.
(ii) The tangent operators $\frac{\mathrm{d}\sigma}{\mathrm{d}\epsilon}$ and $\frac{\mathrm{d}\sigma}{\mathrm{d}T}$ that are necessary for the FE solver to compute the global predictor at the whole FE system's level.

This is usually done through a *return mapping algorithm* (Simo and Hughes, 1998; Praud et al., 2017a,b; Praud, 2018; Chatzigeorgiou et al., 2018), which is detailed in Appendix for the proposed model.

3. Parameters identification for AISI 316L austenitic stainless steel

3.1. Flow stress

The proposed model is identified for the AISI 316L austenitic stainless steel following a specific identification procedure. This is done from monotonic tensile tests taken from literature (Depradeux, 2004; Hendili, 2016). These experiments have been performed at six temperatures ranging from 293 K to 1273 K, and for two strain rates, namely: 2.5×10^{-4} s^{-1} and 2.5×10^{-3} s^{-1}. For each test, the axial plastic strain ε_p is extracted from the experimentally recorded axial stress σ and total strain ε:

$$\varepsilon_p = \varepsilon - \frac{\sigma}{E(T)}, \qquad \text{where} \qquad E(T) = g_e(T) E_0, \tag{27}$$

while the plastic strain rate is assumed to be constant and equal to the strain rate of the test, such that $\dot{\varepsilon}_p \approx \dot{\varepsilon}$. Furthermore, under monotonic uni-axial tension, the plastic strain ε_p equals the multiplier p.

The identification procedure then relies on the evaluation of the flow stress σ as a function of ε_p, where $\dot{\varepsilon}_p$ and T can be regarded as parameters. Based on Eqs. (11) and (15), it yields under monotonic uni-axial conditions, the following relationship between σ, X and $\dot{\varepsilon}_p$:

$$\sigma(X; \dot{\varepsilon}_p, T) = \frac{3}{2} X + \sigma_y(T)\left[1 + (\eta \dot{\varepsilon}_p)^{1/N}\right], \tag{28}$$

whereas the axial back stress X is expressed through Eqs. (7), (13) and (18) and is accordingly governed by the following differential equation:

$$\dot{X} + \left[\gamma \dot{\varepsilon}_p + c(T)\, g_r(T)\, A_X - \frac{g_p'}{g_p}\dot{T}\right] X = c(T)\, \dot{\varepsilon}_p, \tag{29}$$

which can be solved under monotonic conditions at constant temperature ($\dot{T} = 0$). This leads to the following analytical expression:

$$X(\varepsilon_p; \dot{\varepsilon}_p, T) = \frac{c(T)\,\dot{\varepsilon}_p}{\gamma \dot{\varepsilon}_p + c(T)\, g_r(T)\, A_X}\left[1 - \exp\left(-\gamma \varepsilon_p - c(T)\, g_r(T)\, A_X \frac{\varepsilon_p}{\dot{\varepsilon}_p}\right)\right]. \tag{30}$$

Therefore, by inserting (30) into (28), it yields the following expression for the flow stress:

$$\sigma(\varepsilon_p; \dot{\varepsilon}_p, T) = \frac{3}{2}\frac{c(T)\,\dot{\varepsilon}_p}{\gamma \dot{\varepsilon}_p + c(T)\, g_r(T) A_X}\left[1 - \exp\left(-\gamma \varepsilon_p - c(T)\, g_r(T)\, A_X \frac{\varepsilon_p}{\dot{\varepsilon}_p}\right)\right] + \underbrace{\sigma_y(T)\left[1 + (\eta \dot{\varepsilon}_p)^{1/N}\right]}_{\sigma_y^*(T, \dot{\varepsilon}_p)}, \tag{31}$$

where it is recalled that $c(T) = g_p(T) c_0$ and $\sigma_y(T) = g_p(T)\sigma_{y_0}$. In (31), it is important to point out that the last term, namely:

$$\begin{aligned} \sigma_y^*(T, \dot{\varepsilon}_p) &= \sigma_y(T)\left[1 + (\eta \dot{\varepsilon}_p)^{1/N}\right] \\ &= g_p(T)\sigma_{y_0}\left[1 + (\eta \dot{\varepsilon}_p)^{1/N}\right], \end{aligned} \tag{32}$$

can be interpreted as an apparent yield stress, which can be conveniently read on a tensile curve for a given temperature T and plastic strain rate $\dot{\varepsilon}_p$. It is furthermore worth noticing that if the hardening recovery mechanism is not active, which is likely to occur at low temperature, then Eq. (31) is reduced to:

$$\sigma(\varepsilon_p; \dot{\varepsilon}_p, T) = g_p(T)\left[\frac{3}{2}\frac{c_0}{\gamma}\left[1 - \exp\left(-\gamma \varepsilon_p\right)\right] + \sigma_{y_0}\left[1 + (\eta \dot{\varepsilon}_p)^{1/N}\right]\right]. \tag{33}$$

In this condition, one can remark that the $g_p(T)$ acts as a unique shift function to the whole apparent hardening at the reference temperature.

With or without hardening recovery, the assessment of the flow stress conveniently enables to identify the parameters of the model. The identification procedure is then performed according to the three following steps:

(i) Identification of the shift functions $g_e(T)$ and $g_p(T)$ associated with the temperature-dependency of the elastic and viscoplastic properties,
(ii) Identification of the viscoplastic parameters,
(iii) Identification of the hardening recovery parameters,

which are detailed in the next subsections.

3.2. Identification of the shift functions

Prior to identifying the model from the flow stress, it is important to calibrate the shift function $g_e(T)$ and $g_p(T)$ associated with the elastic and viscoplastic properties, respectively, through Eqs. (2), (3) and (12). Although temperature dependencies are commonly formulated using Arrhenius-like law (Lemaitre and Chaboche, 1990), no specific forms have been defined at this stage for these two functions.

In this work, given the experimental data (Depradeux, 2004; Hendili, 2016), a form based on the Langevin-like formulation, as proposed by Kittel et al. (1996), has been considered for

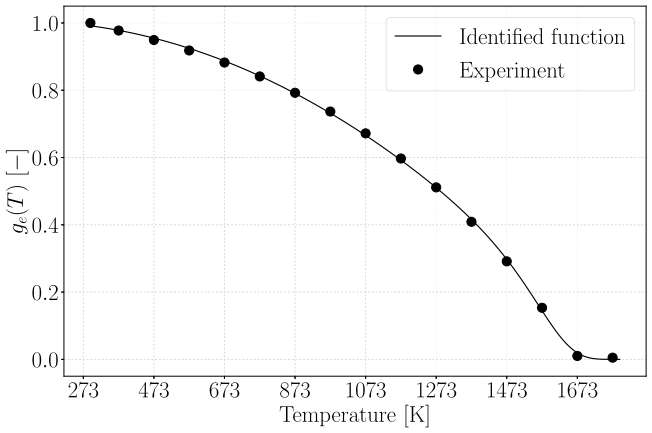

(a) Calibrated function $g_e(T)$ against experiment data.

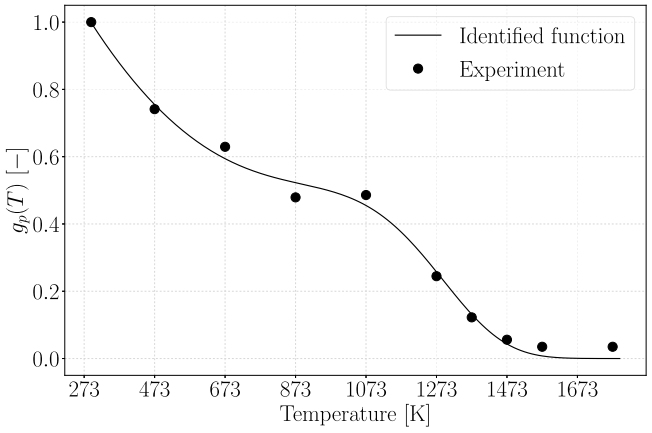

(b) Calibrated function $g_p(T)$ against experiment data

Fig. 4. Shift function $g_e(T)$ and $g_p(T)$ associated with the temperature dependencies of the elastic and viscoplastic properties, respectively. These two functions $g_e(T)$ are calibrated from experimental data taken from Depradeux (2004) and Hendili (2016).

$g_e(T)$. This function employs a multiplicative decomposition of a second order polynomial and exponential function. Accordingly, it reads:

$$g_e(T) = \left(a_1^e + a_2^e\, T + a_3^e\, T^2\right) \times \exp\left(-\left(\frac{T}{T_e}\right)^{n_e}\right), \tag{34}$$

where the parameters a_1^e, a_2^e, a_3^e, n_e, T_e are calibrated from the experimental data by calculating for each test the ratio between the Young's modulus $E(T)$ and the one at the reference temperature E_0. Fig. 4(a) shows the obtained curve for $g_e(T)$ with the identified parameters as well as the experimental data from Depradeux (2004) and Hendili (2016).

Similarly to the elastic properties, the viscoplastic properties are very sensitive to the temperature. For $g_p(T)$, a formulation similar to $g_e(T)$ has been considered to capture the temperature-dependency of the viscoplastic properties. This function introduces another set of material parameters a_1^p, a_2^p, a_3^p, n_p, T_p, such that:

$$g_p(T) = \left(a_1^p + a_2^p\, T + a_3^p\, T^2\right) \times \exp\left(-\left(\frac{T}{T_p}\right)^{n_p}\right), \tag{35}$$

where the calibration is done by calculating for each test the ratio between the apparent yield stress $\sigma_y^*(T, \dot{\varepsilon}_p)$ and the one at room temperature considering the same strain rate, $\sigma_y^*(T_0, \dot{\varepsilon}_p)$, according to Eq. (32). The identified function $g_p(T)$ agrees well with the experimental data from Depradeux (2004) and Hendili (2016) as shown in Fig. 4(b).

Table 2
Identified parameters for AISI 316L austenitic stainless steel.

Feature	Parameter	Value	Unit
Thermo-elasticity	E_0	195 600	MPa
	ν_0	0.3	–
	α	17.1×10^{-6}	K^{-1}
	a_1^e	1.00	–
	a_2^e	6.98×10^{-5}	K^{-1}
	a_3^e	-3.57×10^{-7}	K^{-2}
	n_e	22.4	–
	T_e	1629	K
Thermo-visco-plasticity	c_0	4.0×10^4	MPa
	γ	358	–
	N	10	–
	η	1.45×10^4	s
	σ_{y_0}	100	MPa
	a_1^p	1.61	–
	a_2^p	-2.52×10^{-3}	K^{-1}
	a_3^p	1.54×10^{-6}	K^{-2}
	n_p	6.83	–
	T_p	1234	K
Hardening recovery	A_X	9.76×10^{-4}	$MPa^{-1}\ s^{-1}$
	n_r	11.9	–
	T_r	1234	K

As expected, the apparent yield stress is much more sensitive at low temperatures than the Young's modulus. It can be noticed that $g_p(T)$ exhibits three regimes. At low temperatures (below 673 K), the apparent yield stress decreases about 40 % compared to the reference temperature. Then, at intermediate temperatures between 673 K and 1073 K, the apparent yield stress is halved compared to the reference temperature but it decreases less quickly than for the first regime. Finally, for temperatures above 1073 K, the apparent yield stress drastically drops and nearly vanishes reaching a value close to 0 for temperatures above 1473 K. Although the experimental data are few for the apparent yield stress, it is important to point out that the identified temperature dependency is well consistent with known tendencies for other metallic materials of the same type (Gardner and Baddoo, 2006; Gardner et al., 2010).

3.3. Identification of the viscoplastic parameters

At low temperatures, typically below 873 K, the recovery mechanism can be considered as inactive (Kerrouault, 2001; Depradeux, 2004). Under this condition, as explained in Section 3.1, the expression of the flow stress (33) only involves the shift function $g_p(T)$ and the parameters related to viscoplasticity, namely: σ_{y_0} c_0, γ, η and N. Since $g_p(T)$ is known at this stage, one can identify these parameters by minimizing the least squares between the experimentally recorded stresses at $T < 873$ K and the ones calculated using Eq. (33).

3.4. Identification of the hardening recovery parameters

At high temperatures, typically above 873 K, the hardening recovery mechanism can be considered as active (Kerrouault, 2001; Depradeux, 2004). In this condition, the expression of the flow stress (31) now involves the parameters related to viscoplasticity as well as the one related to the hardening recovery, namely: A_X, n_r and T_r. However, since the shift function $g_p(T)$ and the viscoplasticity parameters are known at this stage, one can identify the hardening recovery parameters by minimizing the least squares between the experimentally recorded stresses at $T > 873$ K and the ones calculated using Eq. (31). The obtained parameters are listed in Table 2 while Figs. 5(a) and 5(b) show good agreements between the stress–strain responses computed with these parameters and the experimental data over the whole temperature range and for the two considered strain-rates.

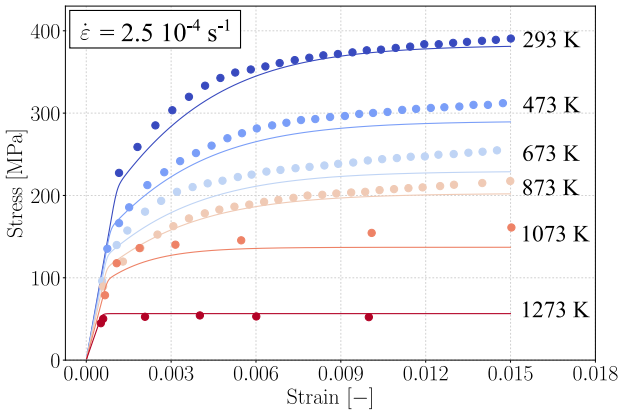

(a) stress-strain responses at $\dot{\varepsilon} = 2.5 \times 10^{-4}$ s^{-1} for various temperatures.

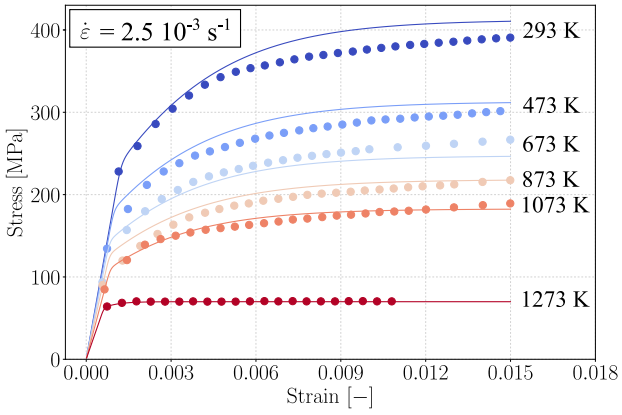

(b) stress-strain responses at $\dot{\varepsilon} = 2.5 \times 10^{-3}$ s^{-1} for various temperatures.

Fig. 5. Comparison between the stress–strain computed responses and the experimental data over the whole temperature range and for the two considered strain-rates, namely: $\dot{\varepsilon} = 2.5 \times 10^{-4}$ s^{-1} and $\dot{\varepsilon} = 2.5 \times 10^{-3}$ s^{-1}. The experimental data, taken from Depradeux (2004) and Hendili (2016), are represented by dot markers whereas the computed responses are depicted by solid lines.

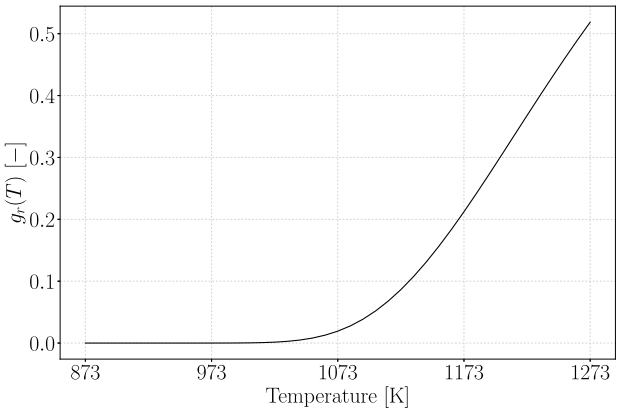

(a) Identified activation function $g_r(T)$ of the hardening recovery mechanism ($T_r = 1234$ K and $n_r = 11.9$).

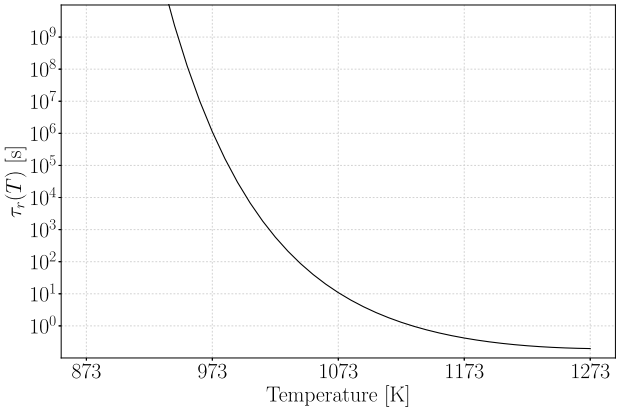

(b) Characteristic time $\tau_r(T)$.

Fig. 6. Identified function $g_r(T)$ and its associated characteristic time $\tau_r(T)$.

Fig. 6(a) displays the identified activation function $g_r(T)$, which is part of the evolution laws of the hardening recovery mechanism through the parameters T_r and n_r (see Sub- Section 2.2.2). It shows that the activation of the recovery mechanism is about 973 K, which is well in line with previous works dealing with this material (Depradeux, 2004; Hendili, 2016; Mouelle et al., 2020).

Fig. 6(b) also shows for reference the characteristic time $\tau_r(T)$ defined in Eq. (20) as a function of the temperature. Below the activation temperature of the recovery mechanism, about 973 K, it appears that τ_r is greater than 10^6 s, which represents about 11 days. Such amount of time is way beyond the time-scale on which thermomechanical loads are usually applied so that the recovery mechanism can be considered as quasi-inactive. The characteristic time τ_r then decreases for higher levels of temperature. Around 1123 K, one can notice that τ_r goes below a second. Such a drastic variation in the recovery kinetics has already been reported for other type of austenitic stainless steels (Taylor and Hodgson, 2011).

Note that, the proposed identification procedure only requires monotonic tension tests, which is sufficient as long as the sole presence of kinematic hardening is assumed. However, it is worth mentioning that, if a combined isotropic-kinematic hardening was considered, a much more complex procedure based on alternate tension–compression tests would certainly be necessary for a proper identification.

4. Validation examples

In this section, three examples of uni-axial simulations are presented to validate the model while providing a better understanding regarding its behaviour. In these examples, the material undergoes hardening recovery under complex thermomechanical loading paths which are of particular interest towards potential applications. The simulations were carried out with the parameters identified in Section 3 for AISI 316L austenitic stainless steel.

4.1. Double hit tension tests

In this example, the so-called *double hit tension test* is applied to the material. Fig. 7 shows that a stress of 300 MPa is first applied in 100 s before being released to zero in the next 100 s, during this first loading stage, the material is kept at room temperature (reference temperature). In a second stage, the material is kept free of stress for a certain period of time during which the temperature is raised up to temperature $T_{\max}$ at the heating rate of 10 K s^{-1}. Once reached this temperature is held constant for a time t_{hold} after which the material is cooled down to room temperature at a cooling rate of -10 K s^{-1}. Now comes the third and last stage in which a stress of 350 MPa is now applied in 100 s and next released during the following 100 s, while the material remains at room temperature.

The *double hit tension test* was first proposed by Mouelle et al. (2020) to dissociate the hardening recovery from viscoplasticity as these mechanisms are separately activated during such a test. Indeed,

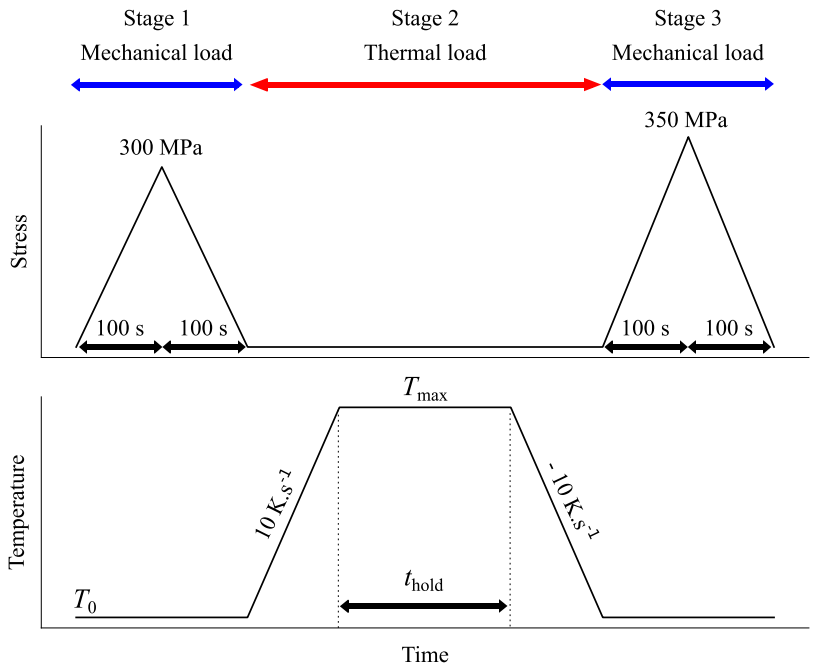

Fig. 7. Thermomechanical loading path for the *double hit tension tests*.

during the first stage, the material yields without any recovery as the temperature is too low. During the second stage, the material is kept at zero stress so that no more plastic strain and hardening can be generated. However, hardening recovery occurs as the temperature increases beyond the activation temperature. During this stage, the amount of recovered hardening depends on the reached temperature T_{max} as well as the time of temperature exposure t_{hold}. The effect of the hardening recovery can then be observed during the third stage, from the level of stress from which the material starts yielding again. If yielding occurs from the stress reached at the first stage, then there is no hardening recovery during the second stage. Contrariwise, if yielding occurs at a lower stress level, then there is hardening recovery, knowing that the initial yielding point can be restored in case of full recovery.

It is recalled that the characteristic time $\tau_r(T)$, given in Eq. (20) and displayed in Fig. 6(b) for the identified set of parameters, is directly related to time that is necessary to fully recover the hardening, *i.e.*, 95 % of the hardening is recovered in $3 \times \tau_r$.

Fig. 8 illustrates a case of a partial recovery. In this simulation, the material is heated slightly above the activation temperature, at T_{max} = 1023 K, which is held for t_{hold} = 100 s. Fig. 8(b) shows that, during the second stage, the hardening was barely recovered as ξ_r slightly increased towards ξ_p. Indeed, in this case, the thermal exposure was too short and too low to achieve full recovery. From an external standpoint, this can be observed at the third stage as the material starts yielding at a stress level nearly equal to the one reached during the first stage, as shown in Fig. 8(a). One can notice that since $\tau_r(T_{max} = 1023\ \text{K}) = 583$ s is much greater than t_{hold} = 100 s. This is well consistent since the hardening was barely recovered for this simulation.

Fig. 9 now illustrates a case of full recovery by increasing the time of temperature exposure to t_{hold} = 3600 s. Fig. 9(b) shows that, in this simulation, the hardening is fully recovered as ξ_r had the time to asymptotically reach ξ_p during the second stage. Therefore during the third stage, the material starts yielding from its initial yielding point, as shown in Fig. 9(a). In this simulation, since $\tau_r(T_{max} = 1023\ \text{K}) = 583$ s is now much shorter than t_{hold} = 3600 s, a full recovery was well expected.

Fig. 10 illustrates another case of full recovery. In this simulation, the material is heated at a higher temperature, namely: T_{max} = 1073 K for t_{hold} = 100 s. In spite of such a short time of exposure, Fig. 10(b)

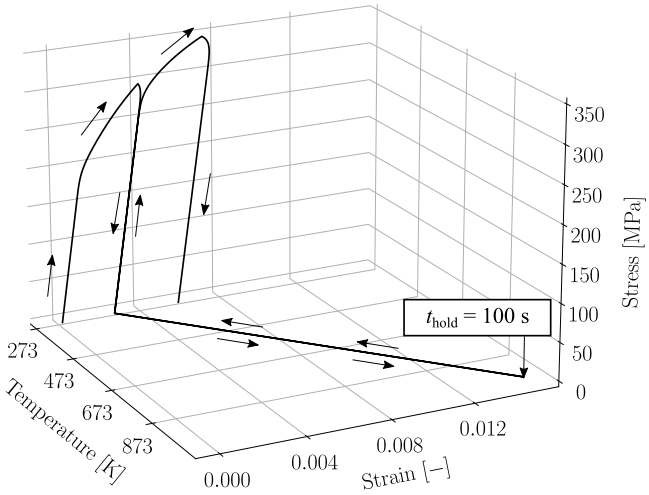

(a) Stress vs. strain vs. temperature.

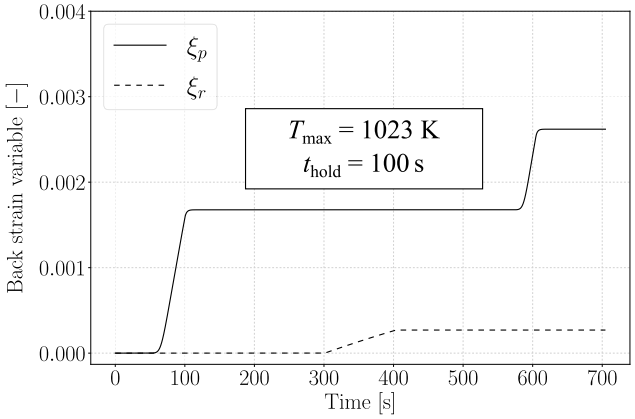

(b) Evolution of the back strain ξ_p and the recovery variable ξ_r.

Fig. 8. *Double hit tension test* for T_{max} = 1023 K and t_{hold} = 100 s.

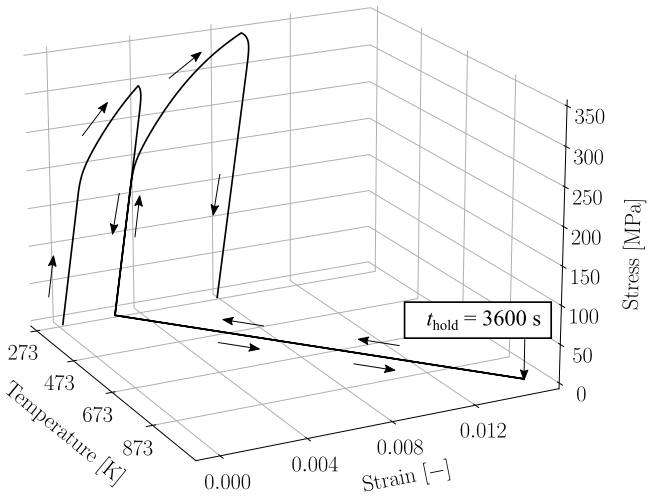

(a) Stress vs. strain vs. temperature.

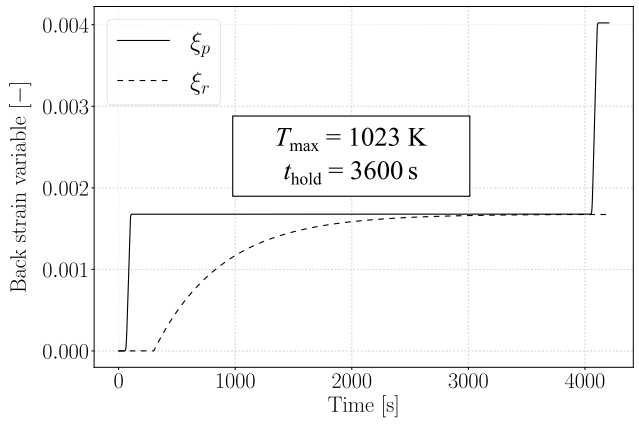

(b) Evolution of the back strain ξ_p and the recovery variable ξ_r.

Fig. 9. *Double hit tension test* for $T_{\text{max}} = 1023$ K and $t_{\text{hold}} = 3600$ s.

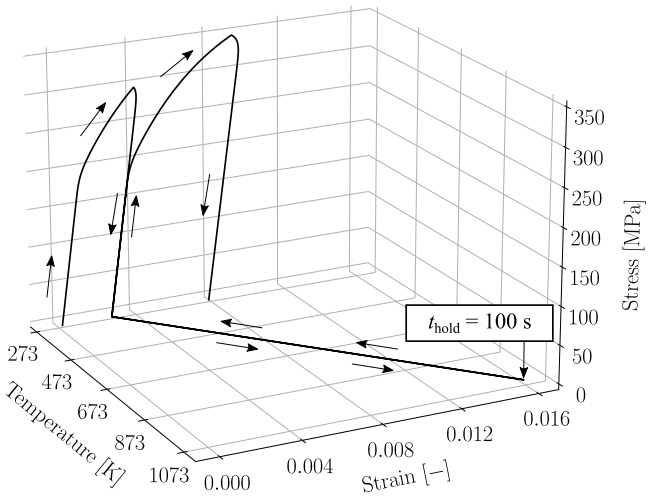

(a) Stress vs. strain vs. temperature.

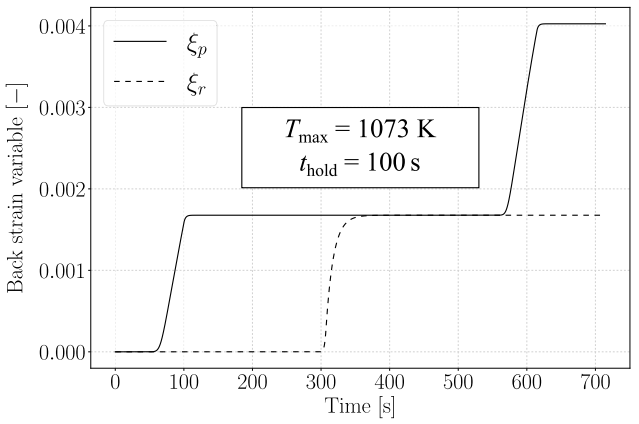

(b) Evolution of the back strain ξ_p and the recovery variable ξ_r.

Fig. 10. *Double hit tension test* for $T_{\text{max}} = 1073$ K and $t_{\text{hold}} = 100$ s.

shows that the higher temperature level results in a much faster recovery, which enables the material to get through to a full recovery and an entire restoration of its yielding point, as depicted in Fig. 10(a). In this simulation, since $\tau_r(T_{\text{max}} = 1073\ \text{K}) = 11$ s is now much shorter than $t_{\text{hold}} = 100$ s, a full recovery was well expected too.

4.2. Stress relaxation tests

In this example, it is proposed to reproduce with the model the *stress relaxation tests* carried out by Depradeux (2004) on AISI 316L austenitic stainless steel. As depicted in Fig. 11, in these experiments, the material is first heated from room temperature up to certain temperature T_{max} under zero stress conditions so that it is free to expand. This temperature is then held constant over the whole remainder of the test. Once at temperature, a strain ε_a is applied at the rate of 2.5×10^{-3} s^{-1} before being held constant for a time t_{hold}. Once this time has elapsed, another ε_a is applied to the material at the same rate.

According the data of Depradeux (2004), two test configurations are considered. In the first one, the material is heated up to $T_{\text{max}} = 473$ K, while an applied strain of $\varepsilon_a = 0.01$ is considered, for an holding time $t_{\text{hold}} = 500$ s. In the second configuration, the material is heated up to $T_{\text{max}} = 1073$ K with an applied strain of $\varepsilon_a = 0.015$, for an holding time $t_{\text{hold}} = 1000$ s.

To further emphasize the role played by the hardening recovery, both configurations are simulated with the proposed model with and

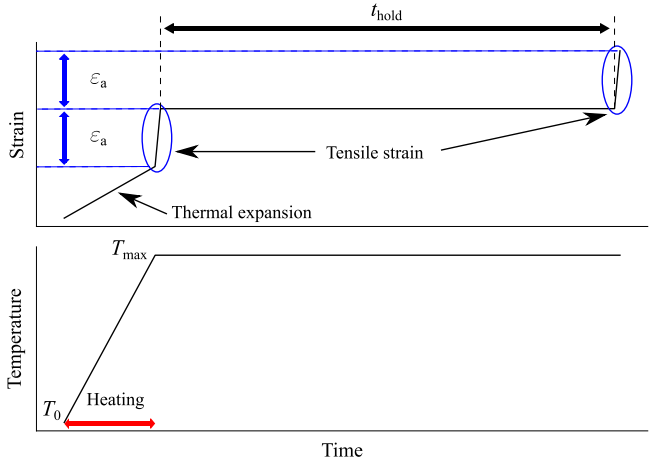

Fig. 11. Thermomechanical loading path for the *stress relaxation tests*.

without hardening recovery. In this latter case, the hardening recovery is turned off by virtually setting the parameter A_X to zero.

Fig. 12 shows the results for the first configuration, for which the temperature remains far below the activation temperature of the hardening recovery mechanism, about 973 K. Therefore, when the

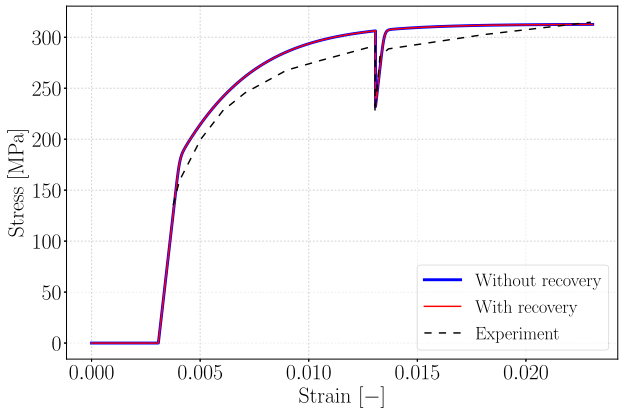

(a) Stress vs. strain. Comparison between the simulation and the experiment by Depradeux (2004).

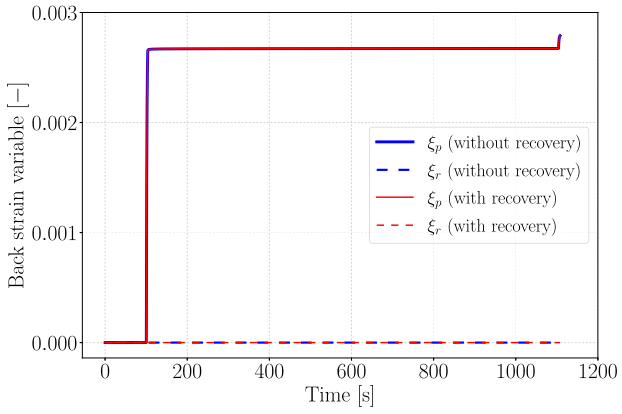

(b) Evolution of the back strain ξ_p and the recovery variable ξ_r.

Fig. 12. *Stress relaxation test* for $T_{\max} = 473$ K, $\varepsilon_a = 0.01$ and $t_{\text{hold}} = 500$ s. Note that, in this case, the applied temperature, *i.e.*, 473 K, is far below the activation temperature of the hardening recovery that is about 973 K.

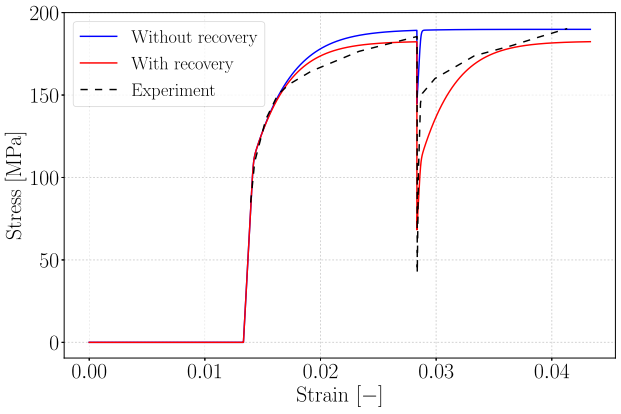

(a) Stress vs. strain. Comparison between the simulation and the experiment by Depradeux (2004).

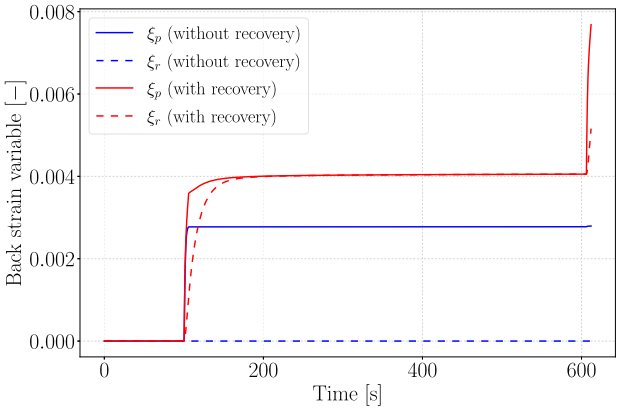

(b) Evolution of the back strain ξ_p and the recovery variable ξ_r.

Fig. 13. *Stress relaxation test* for $T_{\max} = 1073$ K, $\varepsilon_a = 0.015$ and $t_{\text{hold}} = 1000$ s. Note that, in this case, the applied temperature, *i.e.*, 1073 K, is greater than the activation temperature of the hardening recovery that is about 973 K.

strain is held constant, the material exhibits stress relaxation under the sole effect of viscoplasticity. Fig. 12(b) then shows that the recovery variable does not evolve in both simulations with and without recovery, resulting in identical stress–strain responses in Fig. 12(a), which are in relative good agreement with the experimental data.

Fig. 13 now shows the results of the second configuration for which the temperature goes beyond the activation temperature. Thus, the material exhibits stress relaxation resulting from the combined effects of viscoplasticity and the hardening recovery, promoting the development of plastic strain and therefore increasing the amount of relaxed stress. Fig. 13(b) shows that, during the relaxation, the recovery variable ξ_r runs towards the back strain ξ_p while assisting its development. This proceeds up to a point where both variables eventually take the same value. Comparatively with the response without recovery, it can be noticed in Fig. 13(a) that the response with recovery is in much better agreement with the experimental data.

4.3. Satoh test

For this last example, the *Satoh* test carried out by Depradeux (2004), Depradeux and Coquard (2018) on AISI 316L austenitic stainless steel is reproduced with the model. The *Satoh test* is an experiment that is typically representative of the multi-pass welding conditions (Satoh et al., 1966; Satoh and Ohnishi, 1972; Mouelle, 2020). It consists in applying thermal cycles to the material while its axial strain is continuously constrained to zero. In the present case, Fig. 14 shows that four successive cycles are considered. The material is heated at the rate of 90 K s^{-1} from room temperature ($T_0 = 293$ K) up to 1348 K, 1128 K, 908 K and 685 K, for cycle 1, 2, 3 and 4, respectively, and subsequently cooled down to room temperature ($T_0 = 293$ K) at the rate of 0.3 K s^{-1}.

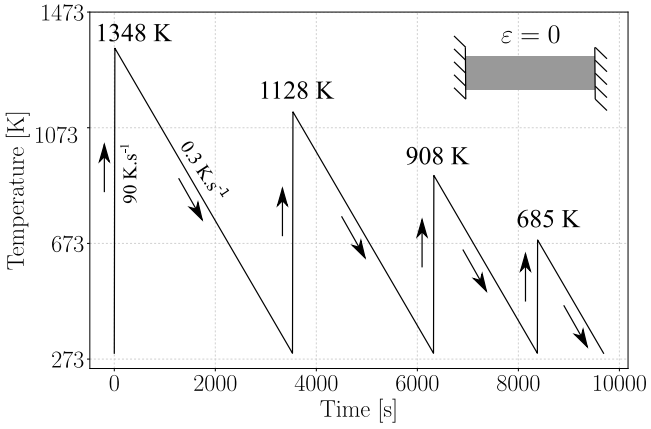

Fig. 14. Thermomechanical loading path for the *Satoh test*.

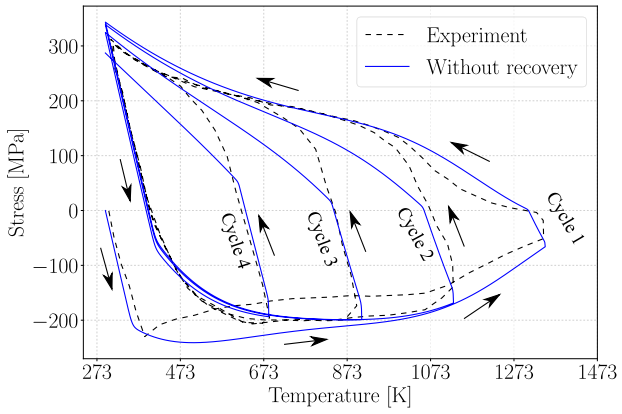

(a) Stress vs. temperature. Comparison between the simulation and the experiment by Depradeux (2004); Depradeux and Coquard (2018).

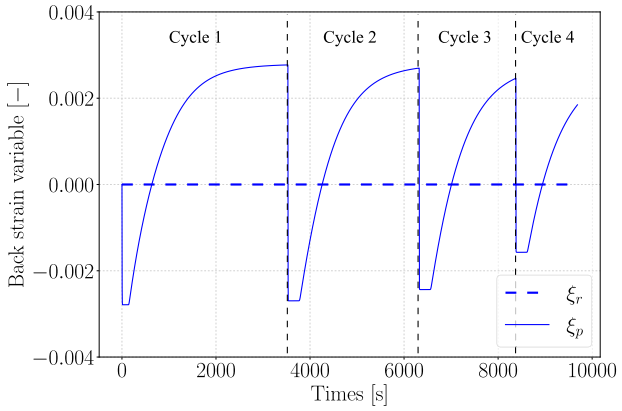

(b) Evolution of the back strain ξ_p and the recovery variable ξ_r.

Fig. 15. *Satoh test* without hardening recovery.

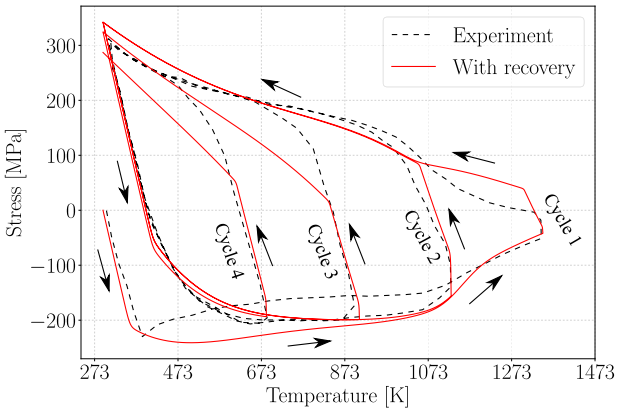

(a) Stress vs. temperature. Comparison between the simulation and the experiment by Depradeux (2004); Depradeux and Coquard (2018).

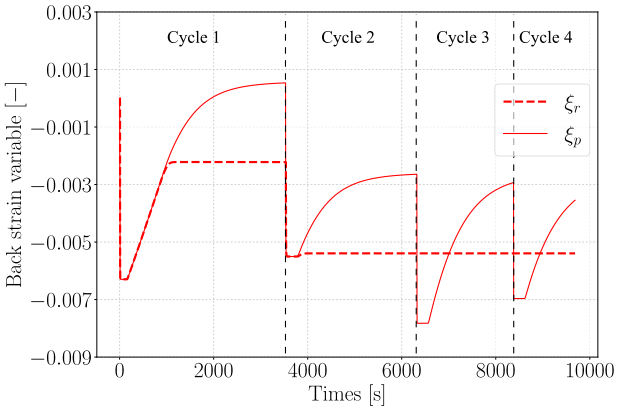

(b) Evolution of the back strain ξ_p and the recovery variable ξ_r.

Fig. 16. *Satoh test* with hardening recovery.

As for the *Stress relaxation test*, the *Satoh test* is simulated with the proposed model with and without hardening recovery. It is recalled that, in this latter case, the hardening recovery is turned off by virtually setting the parameter A_X to zero.

Fig. 15(a) shows the comparison between the experimental data for the *Satoh test* and the simulated stress–temperature response without hardening recovery. During each thermal cycle, as it is prevented to expand, the material undergoes alternate compression and tension states with yielding over the course of the heating and cooling stages, respectively. According to the model, Fig. 15(b) shows that the back strain variable ξ_p makes the yield function shift in compression and in tension during the heating and cooling stages, respectively. Note that the back strain recovery does not evolve here since the hardening recovery is turned off in this simulation. In spite of that, it can be noticed that the model predicts a similar tendency compared to the experiment. During the heating stage of the first thermal cycle (from 293 K to 1348 K), the stress is overestimated of about 50 MPa. Then, during the next cooling stage, (from 1348 K to 293 K), the stress is quite close from the experimental one. For the next cycles, the heating stages are well predicted. However, during the cooling stages, the yielding point occurs sooner than what is experimentally observed.

Fig. 16(a) now shows the comparison between the experimental data and the simulated stress–temperature response with hardening recovery. In this case, the contribution of the hardening recovery allows to improve the prediction at the end of the first heating stage, while the yielding point is slightly shifted at the beginning of the next cooling stage. This greatly improves the prediction during the second cycle whereas the following cycles keep nearly unchanged compared to the simulation without hardening recovery. As depicted in Fig. 16(b), the recovery variable ξ_r evolves towards ξ_p only during the two first cycles for which the temperature exceeds the activation temperature, *i.e.*, about 973 K. During this time, the recovery mechanism tends to bring the yield function back to its state without hardening, counteracting the effect of the latter as it progresses.

5. Conclusions and perspectives

In this work, a new phenomenological model has been proposed to describe the thermally-activated hardening recovery mechanisms in metallic materials. Such a feature constitutes an original modelling approach to capture the effects caused by different phenomena occurring at the microstructure level, such as dislocation annihilations, recrystallization and grain growth. Comparatively to previous works, where the hardening recovery was only considered in a classical plasticity formalism with isotropic hardening (Mouelle et al., 2020), the proposed model rather extends this concept in a viscoplastic formulation with kinematic hardening. Besides, the model also introduces temperature-dependent shift functions to better represent the thermomechanical response of the material over a wide temperature range whether the hardening recovery is active or not. The model's parameters have been successfully identified for AISI 316L austenitic stainless steel through a stepwise identification procedure based on the evaluation of the flow stress, while validation is further achieved on other representative tests,

namely *double hit tension tests*, *stress relaxation tests* and *Satoh tests* for which the material undergoes hardening recovery under complex thermomechanical loading paths.

As future prospects, it is intended to extend the present formulation to combined isotropic-kinematic hardening. Although this might require additional thermomechanical experiments (Thiercelin et al., 2022b) as well as a revised identification procedure, a combined hardening might be helpful to better capture the material's response upon alternate tension–compression like it is the case for the *Satoh test*. Extensions to strain gradient plasticity (Voyiadjis and Song, 2019; Martínez-Pañeda et al., 2019; Jebahi and Forest, 2021) and/or nonlocal damage (Kiefer et al., 2018; Praud et al., 2021; Satouri et al., 2022) are also under consideration to account for strain localization and other size effects. Finally, establishing correlations between microstructural changes and the evolution of the internal state variables (Thiercelin et al., 2020, 2022a) describing the material behaviour at the upper scale would be a valuable information towards enriching the proposed constitutive model.

CRediT authorship contribution statement

Léo Thiercelin: Writing – original draft, Formal analysis, Investigation, Methodology, Validation. **Francis Praud:** Conceptualization, Writing – original draft, Formal analysis, Investigation. **Fodil Meraghni:** Methodology, Formal analysis, Review & editing, Conceptualization. **Eric Fleury:** Methodology, Formal analysis, Review & editing, Conceptualization.

Declaration of competing interest

The authors declare that they have no known competing financial interests or personal relationships that could have appeared to influence the work reported in this paper.

Data availability

Data will be made available on request.

Appendix. Return mapping algorithm

The numerical implementation of the proposed model is based on the *convex cutting plane* form of the *return mapping algorithm*, which is detailed in this appendix. The reader can refer to several references among them (Simo and Hughes, 1998; Praud et al., 2017a,b; Praud, 2018; Chatzigeorgiou et al., 2018).

A.1. Residuals and linearization of the constitutive equations

The evolution laws of the viscoplastic multiplier p and the recovery variable $\boldsymbol{\xi}_r$, given in (15) and (18), respectively, are written under the form of residuals that must both satisfy a nullity condition. Accordingly, this gives:

$$R_p(\dot{p},\boldsymbol{\sigma},\boldsymbol{X},T) = \dot{p} - \frac{1}{\eta}\left[\frac{\left\langle f(\boldsymbol{\sigma},\boldsymbol{X},T)\right\rangle_+}{\sigma_y(T)}\right]^N, \tag{A.1a}$$

$$\boldsymbol{R}_{\xi_r}(\dot{\boldsymbol{\xi}}_r,\boldsymbol{X},T) = \dot{\boldsymbol{\xi}}_r - g_r(T)\boldsymbol{A}_X\boldsymbol{X}. \tag{A.1b}$$

Taken in their linearized forms, it yields:

$$\begin{aligned}\delta R_p &= \frac{\partial R_p}{\partial \dot{p}}\frac{\partial \dot{p}}{\partial p}\delta p + \frac{\partial R_p}{\partial \boldsymbol{\sigma}} : \delta\boldsymbol{\sigma} + \frac{\partial R_p}{\partial \boldsymbol{X}} : \delta\boldsymbol{X} + \frac{\partial R_p}{\partial T}\delta T \\ &= A_{pp}\delta p + \boldsymbol{A}_{p\sigma} : \delta\boldsymbol{\sigma} + \boldsymbol{A}_{pX} : \delta\boldsymbol{X} + A_{pT}\delta T,\end{aligned} \tag{A.2a}$$

$$\begin{aligned}\delta\boldsymbol{R}_{\xi_r} &= \frac{\partial \boldsymbol{R}_{\xi_r}}{\partial \dot{\boldsymbol{\xi}}_r} : \frac{\partial \dot{\boldsymbol{\xi}}_r}{\partial \boldsymbol{\xi}_r} : \delta\boldsymbol{\xi}_r + \frac{\partial \boldsymbol{R}_{\xi_r}}{\partial \boldsymbol{X}} : \delta\boldsymbol{X} + \frac{\partial \boldsymbol{R}_{\xi_r}}{\partial T} : \delta T \\ &= \mathbb{A}_{\xi_r\xi_r} : \delta\boldsymbol{\xi}_r + \mathbb{A}_{\xi_r X} : \delta\boldsymbol{X} + \boldsymbol{A}_{\xi_r T}\delta T.\end{aligned} \tag{A.2b}$$

Let us recall that the *convex cutting plane* method (Simo and Hughes, 1998; Praud et al., 2017a,b; Praud, 2018; Chatzigeorgiou et al., 2018) considers simplified linearized forms of the flow Eqs. (13), which become:

$$\delta\boldsymbol{\varepsilon}_p = \boldsymbol{\Lambda}(\boldsymbol{\sigma},\boldsymbol{X})\delta p, \qquad \delta\boldsymbol{\xi}_p = \boldsymbol{\Omega}(\boldsymbol{\sigma},\boldsymbol{X},T)\delta p, \tag{A.3}$$

so that the linearized stress and back stress, according to Eqs. (6) and (7), are given by:

$$\begin{aligned}\delta\boldsymbol{\sigma} &= \frac{\partial\boldsymbol{\sigma}}{\partial\boldsymbol{\varepsilon}} : \delta\boldsymbol{\varepsilon} + \frac{\partial\boldsymbol{\sigma}}{\partial T}\delta T + \frac{\partial\boldsymbol{\sigma}}{\partial\boldsymbol{\varepsilon}_p} : \delta\boldsymbol{\varepsilon}_p \\ &= \frac{\partial\boldsymbol{\sigma}}{\partial\boldsymbol{\varepsilon}} : \delta\boldsymbol{\varepsilon} + \frac{\partial\boldsymbol{\sigma}}{\partial T}\delta T + \frac{\partial\boldsymbol{\sigma}}{\partial\boldsymbol{\varepsilon}_p} : \boldsymbol{\Lambda}(\boldsymbol{\sigma},\boldsymbol{X})\delta p \\ &= \mathbb{B}_{\sigma\varepsilon} : \delta\boldsymbol{\varepsilon} + \boldsymbol{B}_{\sigma T}\delta T + \boldsymbol{B}_{\sigma p}\delta p,\end{aligned} \tag{A.4}$$

$$\begin{aligned}\delta\boldsymbol{X} &= \frac{\partial\boldsymbol{X}}{\partial T}\delta T + \frac{\partial\boldsymbol{X}}{\partial\boldsymbol{\xi}_p} : \delta\boldsymbol{\xi}_p + \frac{\partial\boldsymbol{X}}{\partial\boldsymbol{\xi}_r} : \delta\boldsymbol{\xi}_r \\ &= \frac{\partial\boldsymbol{X}}{\partial T}\delta T + \frac{\partial\boldsymbol{X}}{\partial\boldsymbol{\xi}_p} : \boldsymbol{\Omega}(\boldsymbol{\sigma},\boldsymbol{X},T)\delta p + \frac{\partial\boldsymbol{X}}{\partial\boldsymbol{\xi}_r} : \delta\boldsymbol{\xi}_r \\ &= \boldsymbol{B}_{XT}\delta T + \boldsymbol{B}_{Xp}\delta p + \mathbb{B}_{X\xi_r} : \delta\boldsymbol{\xi}_r.\end{aligned} \tag{A.5}$$

Thus, inserting (A.4) and (A.5) into (A.2a) and (A.2b) eventually leads to the full linearization of the residuals:

$$\delta R_p = K_{pp}\delta p + \boldsymbol{K}_{p\xi_r} : \delta\boldsymbol{\xi}_r + \boldsymbol{K}_{p\varepsilon} : \delta\boldsymbol{\varepsilon} + K_{pT}\delta T, \tag{A.6a}$$

$$\delta\boldsymbol{R}_{\xi_r} = \boldsymbol{K}_{\xi_r p}\delta p + \mathbb{K}_{\xi_r\xi_r} : \delta\boldsymbol{\xi}_r + \mathbb{K}_{\xi_r\varepsilon} : \delta\boldsymbol{\varepsilon} + \boldsymbol{K}_{\xi_r T}\delta T, \tag{A.6b}$$

or, equivalently:

$$\begin{Bmatrix}\delta R_p \\ \delta\boldsymbol{R}_{\xi_r}\end{Bmatrix} = \begin{pmatrix}K_{pp} & \boldsymbol{K}_{p\xi_r} \\ \boldsymbol{K}_{\xi_r p} & \mathbb{K}_{\xi_r\xi_r}\end{pmatrix} \times \begin{Bmatrix}\delta p \\ \delta\boldsymbol{\xi}_r\end{Bmatrix} + \begin{pmatrix}\boldsymbol{K}_{p\varepsilon} & K_{pT} \\ \mathbb{K}_{\xi_r\varepsilon} & \boldsymbol{K}_{\xi_r T}\end{pmatrix} \times \begin{Bmatrix}\delta\boldsymbol{\varepsilon} \\ \delta T\end{Bmatrix}, \tag{A.7}$$

where

$$K_{pp} = A_{pp} + \boldsymbol{A}_{p\sigma} : \boldsymbol{B}_{\sigma p} + \boldsymbol{A}_{pX} : \boldsymbol{B}_{Xp}, \tag{A.8a}$$

$$\boldsymbol{K}_{p\xi_r} = \boldsymbol{A}_{pX} : \mathbb{B}_{X\xi_r}, \tag{A.8b}$$

$$\boldsymbol{K}_{p\varepsilon} = \boldsymbol{A}_{p\sigma} : \mathbb{B}_{\sigma\varepsilon}, \tag{A.8c}$$

$$K_{pT} = \boldsymbol{A}_{p\sigma} : \boldsymbol{B}_{\sigma T} + \boldsymbol{A}_{pX} : \boldsymbol{B}_{XT} + A_{pT}, \tag{A.8d}$$

$$\boldsymbol{K}_{\xi_r p} = \mathbb{A}_{\xi_r X} : \boldsymbol{B}_{Xp}, \tag{A.8e}$$

$$\mathbb{K}_{\xi_r\xi_r} = \mathbb{A}_{\xi_r\xi_r} + \mathbb{A}_{\xi_r X} : \mathbb{B}_{X\xi_r}, \tag{A.8f}$$

$$\mathbb{K}_{\xi_r\varepsilon} = 0, \tag{A.8g}$$

$$\boldsymbol{K}_{\xi_r T} = \mathbb{A}_{\xi_r X} : \boldsymbol{B}_{XT} + \boldsymbol{A}_{\xi_r T}, \tag{A.8h}$$

with

$$A_{pp} = \frac{\partial R_p}{\partial\dot{p}}\frac{\partial\dot{p}}{\partial p} = \frac{1}{\Delta t}, \tag{A.9a}$$

$$\boldsymbol{A}_{p\sigma} = \frac{\partial R_p}{\partial\boldsymbol{\sigma}} = -\frac{N}{\eta\ \sigma_y(T)}\left[\frac{\left\langle f(\boldsymbol{\sigma},\boldsymbol{X},T)\right\rangle_+}{\sigma_y(T)}\right]^{N-1}\boldsymbol{\Lambda}(\boldsymbol{\sigma},\boldsymbol{X}), \tag{A.9b}$$

$$\boldsymbol{A}_{pX} = \frac{\partial R_p}{\partial\boldsymbol{X}} = \frac{N}{\eta\ \sigma_y(T)}\left[\frac{\left\langle f(\boldsymbol{\sigma},\boldsymbol{X},T)\right\rangle_+}{\sigma_y(T)}\right]^{N-1}\boldsymbol{\Lambda}(\boldsymbol{\sigma},\boldsymbol{X}), \tag{A.9c}$$

$$A_{pT} = \frac{\partial R_p}{\partial T} = \frac{N}{\eta}\left[\frac{\left\langle f(\boldsymbol{\sigma},\boldsymbol{X},T)\right\rangle_+}{\sigma_y(T)}\right]^{N-1}\frac{\sigma_y'(T)\left[\sigma_y(T)+f(\boldsymbol{\sigma},\boldsymbol{X},T)\right]}{\sigma_y(T)^2}, \tag{A.9d}$$

$$\mathbb{A}_{\xi_r\xi_r} = \frac{\partial\boldsymbol{R}_{\xi_r}}{\partial\dot{\boldsymbol{\xi}}_r} : \frac{\partial\dot{\boldsymbol{\xi}}_r}{\partial\boldsymbol{\xi}_r} = \frac{\mathbb{I}}{\Delta t}, \tag{A.9e}$$

$$\mathbb{A}_{\xi_r \boldsymbol{X}} = \frac{\partial \boldsymbol{R}_{\xi_r}}{\partial \boldsymbol{X}} = -g_r(T) A_X \mathbb{I}, \tag{A.9f}$$

$$\boldsymbol{A}_{\xi_r T} = \frac{\partial \boldsymbol{R}_{\xi_r}}{\partial T} = -g_r'(T) A_X \boldsymbol{X}, \tag{A.9g}$$

$$\mathbb{B}_{\boldsymbol{\sigma}\boldsymbol{\varepsilon}} = \frac{\partial \boldsymbol{\sigma}}{\partial \boldsymbol{\varepsilon}} = g_e(T)\ \mathbb{C}_0, \tag{A.9h}$$

$$\boldsymbol{B}_{\boldsymbol{\sigma}T} = \frac{\partial \boldsymbol{\sigma}}{\partial T} = g_e'(T)\ \mathbb{C}_0 : \left(\boldsymbol{\varepsilon} - \boldsymbol{\varepsilon}_p - \boldsymbol{\varepsilon}_{th}(T)\right) - g_e(T)\ \mathbb{C}_0 : \alpha \boldsymbol{I}, \tag{A.9i}$$

$$\boldsymbol{B}_{\boldsymbol{\sigma}p} = \frac{\partial \boldsymbol{\sigma}}{\partial \boldsymbol{\varepsilon}_p} : \boldsymbol{\Lambda}(\boldsymbol{\sigma}, \boldsymbol{X}) = -g_e(T)\ \mathbb{C}_0 : \boldsymbol{\Lambda}(\boldsymbol{\sigma}, \boldsymbol{X}), \tag{A.9j}$$

$$\boldsymbol{B}_{\boldsymbol{X}T} = \frac{\partial \boldsymbol{X}}{\partial T} = g_p'(T)\ c_0\ (\boldsymbol{\xi}_p - \boldsymbol{\xi}_r), \tag{A.9k}$$

$$\boldsymbol{B}_{\boldsymbol{X}p} = \frac{\partial \boldsymbol{X}}{\partial \boldsymbol{\xi}_p} : \boldsymbol{\Omega}(\boldsymbol{\sigma}, \boldsymbol{X}, T) = g_p(T)\ c_0\ \boldsymbol{\Omega}(\boldsymbol{\sigma}, \boldsymbol{X}, T), \tag{A.9l}$$

$$\mathbb{B}_{\boldsymbol{X}\boldsymbol{\xi}_r} = \frac{\partial \boldsymbol{X}}{\partial \boldsymbol{\xi}_r} = -g_p(T)\ c_0\ \mathbb{I}. \tag{A.9m}$$

A.2. Computation of the stress

A.2.1. Elastic prediction with hardening recovery correction

To assess if the material is actively yielding or not, an elastic prediction is necessary. During this step, the internal state variables, $\boldsymbol{\varepsilon}_p$, and $\boldsymbol{\xi}_p$ as well as the viscoplastic multiplier p are kept constant such that: $\boldsymbol{\varepsilon}_p^{(n+1)} = \boldsymbol{\varepsilon}_p^{(n)}$, $\boldsymbol{\xi}_p^{(n+1)} = \boldsymbol{\xi}_p^{(n)}$ and $p^{(n+1)} = p^{(n)}$. However, since the recovery variable $\boldsymbol{\xi}_r$ defines the yielding point while having no influence on the elastic behaviour, it is important to let it evolve during the elastic prediction. Accordingly, after an initialization step in which $\boldsymbol{\xi}_r^{(n+1)(k=0)} = \boldsymbol{\xi}_r^{(n)}$, the recovery variable is computed by means of iterative corrections such that:

$$\boldsymbol{\xi}_r^{(n+1)(k+1)} = \boldsymbol{\xi}_r^{(n+1)(k)} + \delta\boldsymbol{\xi}_r^{(n+1)(k)}, \tag{A.10}$$

where k refers to the correction loop. Then, $\delta\boldsymbol{\xi}_r$ is obtained from the nullity condition of the residual $\boldsymbol{R}_{\xi_r}$ in its linearized form (A.6b), while considering $\delta p = 0$, $\delta\boldsymbol{\varepsilon}_p = \boldsymbol{0}$ and $\delta\boldsymbol{\xi}_p = \boldsymbol{0}$, along with $\delta\boldsymbol{\varepsilon} = \boldsymbol{0}$ and $\delta T = 0$ (all the quantities are taken at $^{(n+1)(k)}$):

$$\boldsymbol{R}_{\xi_r} + \delta\boldsymbol{R}_{\xi_r} = \boldsymbol{0} \quad \Leftrightarrow \quad \delta\boldsymbol{\xi}_r = -\mathbb{K}_{\xi_r\xi_r}^{-1} : \boldsymbol{R}_{\xi_r}. \tag{A.11}$$

Therefore, the correction loop is repeated until reaching convergence, namely, when the residual $\boldsymbol{R}_{\xi_r}$ is sufficiently close to zero. Once converged, the yield function f can be checked to assess whether the material is actively yielding or not:

- If $f < 0$, then the material is not yielding and no more corrections are needed.
- if $f > 0$, then the material is actively yielding and another corrective step is necessary to account for the viscoplasticity in addition to the hardening recovery.

A.2.2. Viscoplastic and hardening recovery correction

If the material is actively yielding, *i.e.*, $f > 0$, then all the internal state variables, $\boldsymbol{\varepsilon}_p$, $\boldsymbol{\xi}_p$ and $\boldsymbol{\xi}_r$ as well as the viscoplastic multiplier p evolve. Accordingly, after an initialization step in which $p^{(n+1)(k=0)} = p^{(n)}$, $\boldsymbol{\varepsilon}_p^{(n+1)(k=0)} = \boldsymbol{\varepsilon}_p^{(n)}$, $\boldsymbol{\xi}_p^{(n+1)(k=0)} = \boldsymbol{\xi}_p^{(n)}$ and $\boldsymbol{\xi}_r^{(n+1)(k=0)} = \boldsymbol{\xi}_r^{(n)}$ and, all these variables are iteratively computed by:

$$p^{(n+1)(k+1)} = p^{(n+1)(k)} + \delta p^{(n+1)(k)}, \tag{A.12a}$$

$$\boldsymbol{\varepsilon}_p^{(n+1)(k+1)} = \boldsymbol{\varepsilon}_p^{(n+1)(k)} + \delta\boldsymbol{\varepsilon}_p^{(n+1)(k)}, \tag{A.12b}$$

$$\boldsymbol{\xi}_p^{(n+1)(k+1)} = \boldsymbol{\xi}_p^{(n+1)(k)} + \delta\boldsymbol{\xi}_p^{(n+1)(k)}, \tag{A.12c}$$

$$\boldsymbol{\xi}_r^{(n+1)(k+1)} = \boldsymbol{\xi}_r^{(n+1)(k)} + \delta\boldsymbol{\xi}_r^{(n+1)(k)}. \tag{A.12d}$$

Then δp and $\delta\boldsymbol{\xi}_r$ are obtained from the nullity condition of the two residuals R_p and $\boldsymbol{R}_{\xi_r}$ in their linearized form (A.7), while considering $\delta\boldsymbol{\varepsilon} = \boldsymbol{0}$ and $\delta T = 0$ (all the quantities are taken at $^{(n+1)(k)}$):

$$\begin{Bmatrix} R_p + \delta R_p = 0 \\ \boldsymbol{R}_{\xi_r} + \delta\boldsymbol{R}_{\xi_r} = \boldsymbol{0} \end{Bmatrix} \quad \Leftrightarrow \quad \begin{Bmatrix} \delta p \\ \delta\boldsymbol{\xi}_r \end{Bmatrix} = -\begin{pmatrix} L_{pp} & \boldsymbol{L}_{p\xi_r} \\ \boldsymbol{L}_{\xi_r p} & \mathbb{L}_{\xi_r\xi_r} \end{pmatrix} \times \begin{Bmatrix} R_p \\ \boldsymbol{R}_{\xi_r} \end{Bmatrix}, \tag{A.13}$$

where

$$\begin{pmatrix} L_{pp} & \boldsymbol{L}_{p\xi_r} \\ \boldsymbol{L}_{\xi_r p} & \mathbb{L}_{\xi_r\xi_r} \end{pmatrix} = \begin{pmatrix} K_{pp} & \boldsymbol{K}_{p\xi_r} \\ \boldsymbol{K}_{\xi_r p} & \mathbb{K}_{\xi_r\xi_r} \end{pmatrix}^{-1}, \tag{A.14}$$

while, according to the *convex cutting plane* method, $\delta\boldsymbol{\varepsilon}_p$ and $\delta\boldsymbol{\xi}_p$ are calculated using Eqs. (A.3). This correction loop is therefore repeated until reaching convergence, namely, when both residuals R_p and $\boldsymbol{R}_{\xi_r}$ are sufficiently close to zero.

A.3. Tangent operators

The tangent operators $\frac{\mathrm{d}\boldsymbol{\sigma}}{\mathrm{d}\boldsymbol{\varepsilon}}$ and $\frac{\mathrm{d}\boldsymbol{\sigma}}{\mathrm{d}T}$ are also required for the FE solver to compute the global predictor at the whole FE system's level. Since, the proposed implementation is based on the *convex cutting plane* form of the *return mapping algorithm* (Simo and Hughes, 1998; Praud et al., 2017a,b; Praud, 2018; Chatzigeorgiou et al., 2018), it utilizes continuous tangent operators. To compute them, one needs to take back the linearized stress:

$$\mathrm{d}\boldsymbol{\sigma} = \mathbb{B}_{\boldsymbol{\sigma}\boldsymbol{\varepsilon}} : \mathrm{d}\boldsymbol{\varepsilon} + \boldsymbol{B}_{\boldsymbol{\sigma}T}\mathrm{d}T + \boldsymbol{B}_{\boldsymbol{\sigma}p}\mathrm{d}p. \tag{A.15}$$

If the material is not actively yielding, *i.e.*, the computation of the stress stopped at the *elastic prediction with hardening recovery correction*, then $\mathrm{d}p = 0$ and the tangent operators are simply given by: $\frac{\mathrm{d}\boldsymbol{\sigma}}{\mathrm{d}\boldsymbol{\varepsilon}} = \mathbb{B}_{\boldsymbol{\sigma}\boldsymbol{\varepsilon}}$ and $\frac{\mathrm{d}\boldsymbol{\sigma}}{\mathrm{d}T} = \boldsymbol{B}_{\boldsymbol{\sigma}T}$. However, if the material is actively yielding, *i.e.*, the computation of the stress went through the *viscoplastic and hardening recovery correction*, then, one must consider the nullity condition of the two residuals R_p and $\boldsymbol{R}_{\xi_r}$ in their linearized forms (A.7), which eventually leads to:

$$\begin{Bmatrix} \mathrm{d}R_p = 0 \\ \mathrm{d}\boldsymbol{R}_{\xi_r} = \boldsymbol{0} \end{Bmatrix} \Leftrightarrow \begin{Bmatrix} \mathrm{d}p \\ \mathrm{d}\boldsymbol{\xi}_r \end{Bmatrix} = -\begin{pmatrix} L_{pp} & \boldsymbol{L}_{p\xi_r} \\ \boldsymbol{L}_{\xi_r p} & \mathbb{L}_{\xi_r\xi_r} \end{pmatrix} \times \begin{pmatrix} \boldsymbol{K}_{p\varepsilon} & K_{pT} \\ \mathbb{K}_{\xi_r\varepsilon} & \boldsymbol{K}_{\xi_r T} \end{pmatrix} \times \begin{Bmatrix} \mathrm{d}\boldsymbol{\varepsilon} \\ \mathrm{d}T \end{Bmatrix} \tag{A.16}$$

or, equivalently:

$$\mathrm{d}p = \boldsymbol{X}_{p\varepsilon} : \mathrm{d}\boldsymbol{\varepsilon} + X_{pT}\mathrm{d}T, \tag{A.17a}$$

$$\mathrm{d}\boldsymbol{\xi}_r = \mathbb{X}_{\xi_r\varepsilon} : \mathrm{d}\boldsymbol{\varepsilon} + \boldsymbol{X}_{\xi_r T}\mathrm{d}T, \tag{A.17b}$$

where

$$\boldsymbol{X}_{p\varepsilon} = -L_{pp}\boldsymbol{K}_{p\varepsilon} - \boldsymbol{L}_{p\xi_r} : \mathbb{K}_{\xi_r\varepsilon}, \tag{A.18a}$$

$$X_{pT} = -L_{pp}K_{pT} - \boldsymbol{L}_{p\xi_r} : \boldsymbol{K}_{\xi_r T}, \tag{A.18b}$$

$$\mathbb{X}_{\xi_r\varepsilon} = -\boldsymbol{L}_{\xi_r p} \otimes \boldsymbol{K}_{p\varepsilon} - \mathbb{L}_{\xi_r\xi_r} : \mathbb{K}_{\xi_r\varepsilon}, \tag{A.18c}$$

$$\boldsymbol{X}_{\xi_r T} = -\boldsymbol{L}_{\xi_r p}K_{pT} - \mathbb{L}_{\xi_r\xi_r} : \boldsymbol{K}_{\xi_r T}. \tag{A.18d}$$

Thus, by inserting (A.17a) into (A.15), one can identify the tangent operators that are finally given by:

$$\frac{\mathrm{d}\boldsymbol{\sigma}}{\mathrm{d}\boldsymbol{\varepsilon}} = \mathbb{B}_{\boldsymbol{\sigma}\boldsymbol{\varepsilon}} + \boldsymbol{B}_{\boldsymbol{\sigma}p} \otimes \boldsymbol{X}_{p\varepsilon}, \tag{A.19a}$$

$$\frac{\mathrm{d}\boldsymbol{\sigma}}{\mathrm{d}T} = \boldsymbol{B}_{\boldsymbol{\sigma}T} + \boldsymbol{B}_{\boldsymbol{\sigma}p}X_{pT}. \tag{A.19b}$$

References

Angkurarach, L., Juijerm, P., 2020. Effects of high-temperature deep rolling on fatigue, work hardening, and residual stress relaxation of martensitic stainless steel AISI 420. J. Mater. Eng. Perform. 29 (2), 1416–1423. http://dx.doi.org/10.1007/s11665-020-04656-6.

Armstrong, P.J., Frederick, C.O., 1966. A mathematical representation of the multiaxial bauschinger effect. Technical Report RD/B/N731, Central Electricity Generating Board, Berkeley Nuclear Laboratories, UK, p. 24.

Avrami, M., 1939. Kinetics of phase change. I General theory. J. Chem. Phys. 7 (12), 1103–1112. http://dx.doi.org/10.1063/1.1750380.

Avrami, M., 1940. Kinetics of phase change. II Transformation-time relations for random distribution of nuclei. J. Chem. Phys. 8 (2), 212–224. http://dx.doi.org/10.1063/1.1750631.

Besson, J., Cailletaud, G., Chaboche, J., Forest, S., 2010. Non-Linear Mechanics of Materials. In: Solid Mechanics and Its Applications, vol. 167, Springer Netherlands, Dordrecht, http://dx.doi.org/10.1007/978-90-481-3356-7.

Blaizot, J., Chaise, T., Nélias, D., Perez, M., Cazottes, S., Chaudet, P., 2016. Constitutive model for nickel alloy 690 (Inconel 690) at various strain rates and temperatures. Int. J. Plast. 80, 139–153. http://dx.doi.org/10.1016/j.ijplas.2015.08.010.

Chaboche, J., 2008. A review of some plasticity and viscoplasticity constitutive theories. Int. J. Plast. 24 (10), 1642–1693. http://dx.doi.org/10.1016/j.ijplas.2008.03.009.

Chaboche, J.L., Nouailhas, D., 1989. A unified constitutive model for cyclic viscoplasticity and its applications to various stainless steels. J. Eng. Mater. Technol. 111 (4), 424–430. http://dx.doi.org/10.1115/1.3226490.

Chatzigeorgiou, G., Charalambakis, N., Chemisky, Y., Meraghni, F., 2016. Periodic homogenization for fully coupled thermomechanical modeling of dissipative generalized standard materials. Int. J. Plast. 81, 18–39.

Chatzigeorgiou, G., Charalambakis, N., Chemisky, Y., Meraghni, F., 2018. Thermomechanical Behavior of Dissipative Composite Materials. ISTE Press - Elsevier, London.

Deng, D., Zhang, C., Pu, X., Liang, W., 2017. Influence of material model on prediction accuracy of welding residual stress in an austenitic stainless steel multi-pass butt-welded joint. J. Mater. Eng. Perform. 26 (4), 1494–1505. http://dx.doi.org/10.1007/s11665-017-2626-6.

Depradeux, L., 2004. Simulation numérique du soudage - acier 316L : Validation sur cas tests de complexité croissante (Ph.D. thesis). INSA Lyon, France.

Depradeux, L., Coquard, R., 2018. Influence of viscoplasticity, hardening, and annealing effects during the welding of a three-pass slot weld (NET-TG4 round robin). Int. J. Press. Vessels Pip. 164, 39–54. http://dx.doi.org/10.1016/j.ijpvp.2017.04.005.

Estrin, Y., Mecking, H., 1984. A unified phenomenological description of work hardening and creep based on one-parameter models. Acta Metall. 32 (1), 57–70. http://dx.doi.org/10.1016/0001-6160(84)90202-5.

Fanfoni, M., Tomellini, M., 1998. The Johnson–Mehl-Avrami–Kolmogorov model: A brief review. pp. 7–8.

Farzadi, A., 2015. Modeling of isothermal recovery and recrystallization kinetics by means of hardness measurements 46(12). pp. 1218–1225. http://dx.doi.org/10.1002/mawe.201500445.

Gardner, L., Baddoo, N., 2006. Fire testing and design of stainless steel structures. J. Construct. Steel Res. 62 (6), 532–543. http://dx.doi.org/10.1016/j.jcsr.2005.09.009.

Gardner, L., Insausti, A., Ng, K., Ashraf, M., 2010. Elevated temperature material properties of stainless steel alloys. J. Construct. Steel Res. 66 (5), 634–647. http://dx.doi.org/10.1016/j.jcsr.2009.12.016.

Hendili, S., 2016. HSNV140 - thermo-plasticité avec restauration d'écrouissage : essai de dilatométrie bloquée. Technical Report V7.22.140. EDF, p. 15.

Humphreys, F., 1997. A unified theory of recovery, recrystallization and grain growth, based on the stability and growth of cellular microstructures—I. The basic model. Acta Mater. 45 (10), 4231–4240. http://dx.doi.org/10.1016/S1359-6454(97)00070-0.

Humpreys, J., Rohrer, G., Rollet, A., 2017. Recrystallization and Related Annealing Phenomena. Elsevier, http://dx.doi.org/10.1016/B978-0-08-098235-9.01001-6.

Jebahi, M., Forest, S., 2021. Scalar-based strain gradient plasticity theory to model size-dependent kinematic hardening effects. Contin. Mech. Thermodyn. 33, 1223–1241. http://dx.doi.org/10.1007/s00161-020-00967-0.

Karvan, P., Varvani-Farahani, A., 2019a. Ratcheting assessment of visco-plastic alloys at ambient temperature by means of the A-V and O-W hardening rule frameworks. Mech. Mater. 130, 95–104. http://dx.doi.org/10.1016/j.mechmat.2019.01.007.

Karvan, P., Varvani-Farahani, A., 2019b. Time-dependent ratcheting assessment of steel samples undergoing multi-step loading cycles through use of hardening rules. Mater. Today Commun. 21, 100682. http://dx.doi.org/10.1016/j.mtcomm.2019.100682.

Karvan, P., Varvani-Farahani, A., 2020. Viscoplastic ratcheting response of materials under step-loading conditions at various cyclic stress levels. J. Mater. Eng. Perform. 29 (2), 1124–1134. http://dx.doi.org/10.1007/s11665-020-04628-w.

Kerrouault, N., 2001. Fissuration à chaud en soudage d'un acier inoxydable austénitique (Ph.D. thesis). Centrale Paris.

Kiefer, B., Waffenschmidt, T., Sprave, L., Menzel, A., 2018. A gradient-enhanced damage model coupled to plasticity-multi-surface formulation and algorithmic concepts. Int. J. Damage Mech. 27, 253–295. http://dx.doi.org/10.1177/1056789516676306.

Kittel, C., McEuen, P., McEuen, P., 1996. Introduction to Solid State Physics, Vol. 8. Wiley New York.

Kocks, U.F., Mecking, H., 2003. Physics and phenomenology of strain hardening: The FCC case. Prog. Mater. Sci. 48 (3), 171–273. http://dx.doi.org/10.1016/S0079-6425(02)00003-8.

Lemaitre, J., Chaboche, J., 1990. Mechanics of Solid Materials. Cambridge University Press, Cambridge, http://dx.doi.org/10.1017/CBO9781139167970.

Lin, Y.C., Dong, W.-Y., Zhou, M., Wen, D.X., Chen, D.-D., 2018. A unified constitutive model based on dislocation density for an Al-Zn-Mg-Cu alloy at time-variant hot deformation conditions. Mater. Sci. Eng. A 718, 165–172. http://dx.doi.org/10.1016/j.msea.2018.01.109.

Martínez-Pañeda, E., Deshpande, V.S., Niordson, C.F., Fleck, N.A., 2019. The role of plastic strain gradients in the crack growth resistance of metals. J. Mech. Phys. Solids 126, 136–150. http://dx.doi.org/10.1016/j.jmps.2019.02.011.

Mecking, H., Kocks, U.F., 1981. Kinetics of flow and strain-hardening. Acta Metall. 29 (11), 1865–1875. http://dx.doi.org/10.1016/0001-6160(81)90112-7.

Mouelle, L., 2020. Caractérisation et modélisation d'assemblages de tôles en acier inoxydable austénitique brasées et soudées pour des applications d'échangeurs de chaleur (Ph.D. thesis). Laboratoire d'Etude des Microstructures et de Mécanique des Matériaux (LEM3), Metz, France.

Mouelle, L., Praud, F., Chatzigeorgiou, G., Meraghni, F., Serri, J., Fleury, E., 2020. Thermally-activated hardening recovery of thermo-elasto-plastic metals during annealing: constitutive modeling for the simulation of welding process. Mech. Mater. 140, 103218. http://dx.doi.org/10.1016/j.mechmat.2019.103218.

Muránsky, O., Hamelin, C.J., Smith, M.C., Bendeich, P.J., Edwards, L., 2012a. The effect of plasticity theory on predicted residual stress fields in numerical weld analyses. Comput. Mater. Sci. 54, 125–134. http://dx.doi.org/10.1016/j.commatsci.2011.10.026.

Muránsky, O., Smith, M., Bendeich, P., Holden, T., Luzin, V., Martins, R., Edwards, L., 2012b. Comprehensive numerical analysis of a three-pass bead-in-slot weld and its critical validation using neutron and synchrotron diffraction residual stress measurements. Int. J. Solids Struct. 49 (9), 1045–1062. http://dx.doi.org/10.1016/j.ijsolstr.2011.07.006.

Norton, F.H., 1929. The Creep of Steel at High Temperatures. McGraw-Hill Book Co., New York.

Petkovic, R., Luton, M., Jonas, J., 1979. Recovery and recrystallization of polycrystalline copper after hot working. Acta Metall. 27 (10), 1633–1648. http://dx.doi.org/10.1016/0001-6160(79)90045-2.

Praud, F., 2018. Multi-Scale Modelling of Thermoplastic-Based Woven Composites, Cyclic and Time-Dependent Behaviour (Ph.D. thesis). Arts et Métiers Institue of Technology, France.

Praud, F., Chatzigeorgiou, G., Bikard, J., Meraghni, F., 2017a. Phenomenological multi-mechanisms constitutive modelling for thermoplastic polymers, implicit implementation and experimental validation. Mech. Mater. 114, 9–29. http://dx.doi.org/10.1016/j.mechmat.2017.07.001.

Praud, F., Chatzigeorgiou, G., Chemisky, Y., Meraghni, F., 2017b. Hybrid micromechanical-phenomenological modelling of anisotropic damage and anelasticity induced by micro-cracks in unidirectional composites. Compos. Struct. 182, 223–236. http://dx.doi.org/10.1016/j.compstruct.2017.09.013.

Praud, F., Schmitt, T., Zabeida, O., Maïza, S., Martinu, L., Lévesque, M., 2021. Phase field fracture models to predict crack initiation and propagation in anti-reflective coatings. Thin Solid Films 736, 138920. http://dx.doi.org/10.1016/j.tsf.2021.138920.

Satoh, K., Matsui, S., Machida, T., 1966. Thermal stresses developed in high-strength steels subjected to thermal cycles simulating weld heat-affected zone. J. Japan Weld. Soc. 35 (9), 780–789.

Satoh, K., Ohnishi, T., 1972. Transient thermal stresses ofweld heat-affected zone by both-ends fixed bar analogy. Trans. Japan Wel. Soc. 3, 125–134.

Satouri, S., Chatzigeorgiou, G., Benaarbia, A., Meraghni, F., 2022. A gradient enhanced constitutive framework for the investigation of ductile damage localization within semicrystalline polymers. Int. J. Damage Mech. http://dx.doi.org/10.1177/10567895221115459.

Shekarian, A., Varvani-Farahani, A., 2019. Ratcheting prediction at the notch root of steel samples over asymmetric loading cycles. J. Eng. Mater. Technol. 142 (2), http://dx.doi.org/10.1115/1.4045363.

Simo, J.C., Hughes, T.J.R., 1998. Computational Inelasticity. Springer-Verlag, New York.

Suo, L., Weiqi, C., Long, H., Dean, D., 2020. Influence of strain hardening and annealing effect on the prediction of welding residual stresses in a thick-wall 316 stainless steel butt-welded pipe joint. Acta Metall. Sin. 57 (12), 14.

Taylor, A., Hodgson, P., 2011. The post-deformation recrystallization behaviour of 304 stainless steel following high strain rate deformation. Mater. Sci. Eng. A 529, 164–169. http://dx.doi.org/10.1016/j.msea.2011.09.013.

Thiercelin, L., Cazottes, S., Merino, P., Saulot, A., Lebon, F., 2022a. Mechanical white etching layer formation kinetics in pearlitic steels: A phenomenological model based on microstructural characterization. Wear 204585. http://dx.doi.org/10.1016/j.wear.2022.204585.

Thiercelin, L., Cazottes, S., Saulot, A., Lebon, F., Mercier, F., Le Bourlot, C., Dancette, S., Fabrègue, D., 2022b. Development of temperature-controlled shear tests to reproduce white-etching-layer formation in pearlitic rail steel. Materials 15 (19), 6590. http://dx.doi.org/10.3390/ma15196590.

Thiercelin, L., Saint-Aimé, L., Lebon, F., Saulot, A., 2020. Thermomechanical modelling of the tribological surface transformations in the railroad network (White eching layer). Mech. Mater. 103636. http://dx.doi.org/10.1016/j.mechmat.2020.103636.

Totten, G.E., Howes, M.A.H., Inoue, T. (Eds.), 2002. Handbook of Residual Stress and Deformation of Steel. ASM International, Materials Park, Ohio.

Voyiadjis, G.Z., Abed, F.H., 2005. Effect of dislocation density evolution on the thermomechanical response of metals with different crystal structures at low and high strain rates and temperatures. p. 45.

Voyiadjis, G.-Z., Song, Y., 2019. Strain gradient continuum plasticity theories: Theoretical, numerical and experimental investigations. Int. J. Plast. 121, 21–75. http://dx.doi.org/10.1016/j.ijplas.2019.03.002.

Voyiadjis, G.Z., Song, Y., Rusinek, A., 2019. Constitutive model for metals with dynamic strain aging. Mech. Mater. 129, 352–360. http://dx.doi.org/10.1016/j.mechmat.2018.12.012.

Withers, P.J., 2007. Residual stress and its role in failure. Rep. Progr. Phys. 70 (12), 2211–2264. http://dx.doi.org/10.1088/0034-4885/70/12/R04.

Yuan, K., Guo, W., Li, P., Zhang, Y., Li, X., Lin, X., 2019. Thermomechanical behavior of laser metal deposited inconel 718 superalloy over a wide range of temperature and strain rate: testing and constitutive modeling. Mech. Mater. 135, 13–25. http://dx.doi.org/10.1016/j.mechmat.2019.04.024.